International Journal of Refractory Metals and Hard Materials 112 (2023) 106120

Contents lists available at ScienceDirect

International Journal of Refractory Metals and Hard Materials

journal homepage: www.elsevier.com/locate/IJRMHM

Evolution of dislocations and grain boundaries during multi-axial forging of tantalum

A. Kedharnath [a,b], Rajeev Kapoor [a,b,*], Apu Sarkar [a,b]

[a] Mechanical Metallurgy Division, Bhabha Atomic Research Center, Mumbai 400085, India
[b] Division of Engineering Sciences, Homi Bhabha National Institute, Anushaktinagar, Mumbai 400094, India

ARTICLE INFO

Keywords:
Multi-axial forging
Tantalum
Mechanical properties
Ultra-fine grained microstructure
Grain boundary mobility
Molecular dynamics

ABSTRACT

Presented here is the evolution of microstructure of Ta during multi-axial forging, with a specific understanding of how grain boundary movement and their interaction occurs during deformation. Coarse grained (CG) tantalum was multi-axially forged till 3, 6, and 9 passes in a closed channel die to refine grain size and increase its strength. The grain size was refined from 64 μm to 760 nm, the dislocation density increased by an order of magnitude, the Vickers hardness increased from 92 to 223 HV, and the yield strength at room temperature increased from 178 to 653 MPa. It was found that the contribution of GBs to strengthening was higher than that of dislocations. Mechanisms for GB structure evolution during deformation were studied using molecular dynamics (MD) simulations. GB mobility was high for low angle GBs (LAGBs) and reduced with increasing tilt angle, after which it took on low values for high angle GBs (HAGBs). The mobility of specific HAGBs were due to the formation of ledges/disconnections and dissociation into other GB types. MD results showed that the decrease in fraction of HAGBs during initial deformation can be attributed to the dissociation of HAGBs with low mobility into GBs with higher mobility.

1. Introduction

Severe plastic deformation (SPD) is an established technique to impart large strains with the aim of refining the microstructure so as to improve its strength [1–11]. SPD processes such as equal channel angular pressing (ECAP), high pressure torsion (HPT), multi-axial forging (MAF) and accumulative roll bonding (ARB) produce microstructures with ultra-fine grains (UFG) [4,12–14], thereby increasing strength in accordance with the Hall-Petch relation [15]. Apart from reducing the grain size, the process of SPD results in a significant increase in dislocation density ρ of the order of 10^{15} m^{-2}, and is probably an important factor in the strengthening of materials [16]. However, in some metals it has been seen that beyond a certain strain imparted during SPD, the material no longer hardens but starts to soften, as was observed in the case of Al subjected to MAF [17]. This was attributed to the increase in the fraction of high angle grain boundaries (f_{hagb}) and reduction in ρ [17]. As each of the SPD processes takes different strain paths, it is expected that the rate and efficiency of grain refinement varies. Along with the grain size and ρ, crystallographic texture also plays an important role towards strengthening or softening of the material.

MAF is a simple process of sequentially compressing the sample along three orthogonal directions [16–19]. MAF in a confined channel die is a plane strain condition similar to rolling [16,19], and has been carried on many metallic systems such as Cu [18], Al [17], Al–2.5 Mg [19], steels [20–24], Mg alloys [25–29], Nb—1Zr [16], and Ni alloy [30,31], with a resultant increase in strength. Of the various metallic systems listed here, little work in terms of SPD has been carried out on refractory metals [16]. Apart from Zr [32] and Nb—1Zr [16], MAF of other refractory alloys has not been reported. Of the various refractory metals, tantalum and its alloys are of interest as these are used in electronics, medical [33,34], nuclear [35–41], aerospace [37], and defence [33,42] applications for their excellent properties such as corrosion resistance [33,37,43–45], biocompatibility [33,34], resistance to grain growth at elevated temperature [33,46,47], and good ductility at low temperatures. There are some studies in which ECAP and HPT have been carried out on Ta that has resulted in improved properties [48,49]. In both ECAP and HPT the strain state is simple shear, whereas in MAF it is plane strain [14,18,22,23]. Therefore, it is worth investigating the properties of Ta after SPD through MAF. The proposed grain refinement mechanism during SPD [30,50,51], involve cell formation followed by sub-grains and then with further increase of

* Corresponding author at: Mechanical Metallurgy Division, Bhabha Atomic Research Center, Mumbai 400085, India.
E-mail address: rkapoor@barc.gov.in (R. Kapoor).

https://doi.org/10.1016/j.ijrmhm.2023.106120
Received 12 October 2022; Received in revised form 4 January 2023; Accepted 15 January 2023
Available online 25 January 2023
0263-4368/© 2023 Elsevier Ltd. All rights reserved.

strain the formation of high angle grain boundaries (HAGBs). The migration of grain boundaries (GBs), their interaction with dislocation motion and their arrangement also plays a role in refining the microstructure. A review of the SPD processes, the microstructural evolution and their mechanical properties is given in references [16, 52]. In one study GB migration has been seen to affect the recrystallization of grains [53]. The recent work on evolution of GBs under lateral strains suggest that along with grain boundary energy (GBE), there exist external driving force that destabilize the planar GBs [54]. GB migration is one of the important deformation mechanism in nanocrystalline materials [55,56].

The present work demonstrates the evolution of microstructure and their correlation with mechanical properties during MAF of Ta carried out at room temperature. Microstructural characterization includes grain size, estimation of ρ, and texture using electron back scattered diffraction (EBSD) methods. Mechanical characterization includes microhardness, compressive flow stress, and strain rate sensitivity. Molecular dynamics (MD) simulations were performed to bring out the understanding on the movement, interaction and evolution of GBs, such as pinching of GBs, formation of shear bands, and annihilation of grain boundary dislocations (GBD) during plastic deformation.

2. Methodology

2.1. Material and multi-axial forging

Pure Ta rod was used for the current study; its elemental composition is Nb - 45 wppm, W – 33 wppm, Fe – 1 wppm, Ti – 1 wppm, Si – 1 wppm, Mo – 1 wppm, Ni – 1 wppm, O – 87 wppm, H – 5 wppm, N – 2 wppm, C – 28 wppm, and Ta - remaining. The microstructure of the initial material was examined under scanning electron microscope (SEM) to confirm coursed grained (CG) structure with minimal dislocation density. Inverse pole figure (IPF) map and kernel average misorientation (KAM) map of the CG Ta is shown in Fig. 1. CG sample had low in-grain misorientation and an average grain diameter of ~64 μm. The grain size is characterized by the equivalent grain diameter which is calculated from the area of the circle equivalent to the area of any observed grain and is hereafter referred here as 'grain diameter'. The schematic illustration of MAF process is shown in Fig. 2a-c. MAF process was carried out using a die with channel of cross section 10 × 10 mm^2, top plunger, and bottom plug. Pure Ta sample of height 10 mm, thickness 9.9 mm, and width 5 mm was placed inside the channel between the plunger and plug such that the sample dimension of 9.9 mm goes into 10 mm side of the channel.

Each pressing reduced the sample height to 50% along the sample dimension of 10 mm which counts as one MAF pass. The samples were forged to 3, 6, and 9 passes and are designated as 3P, 6P, and 9P, respectively. The MAF was carried out at room temperature with crosshead velocity of 2 mm/min. The effective strain ε_{eff} after each MAF pass was calculated using,

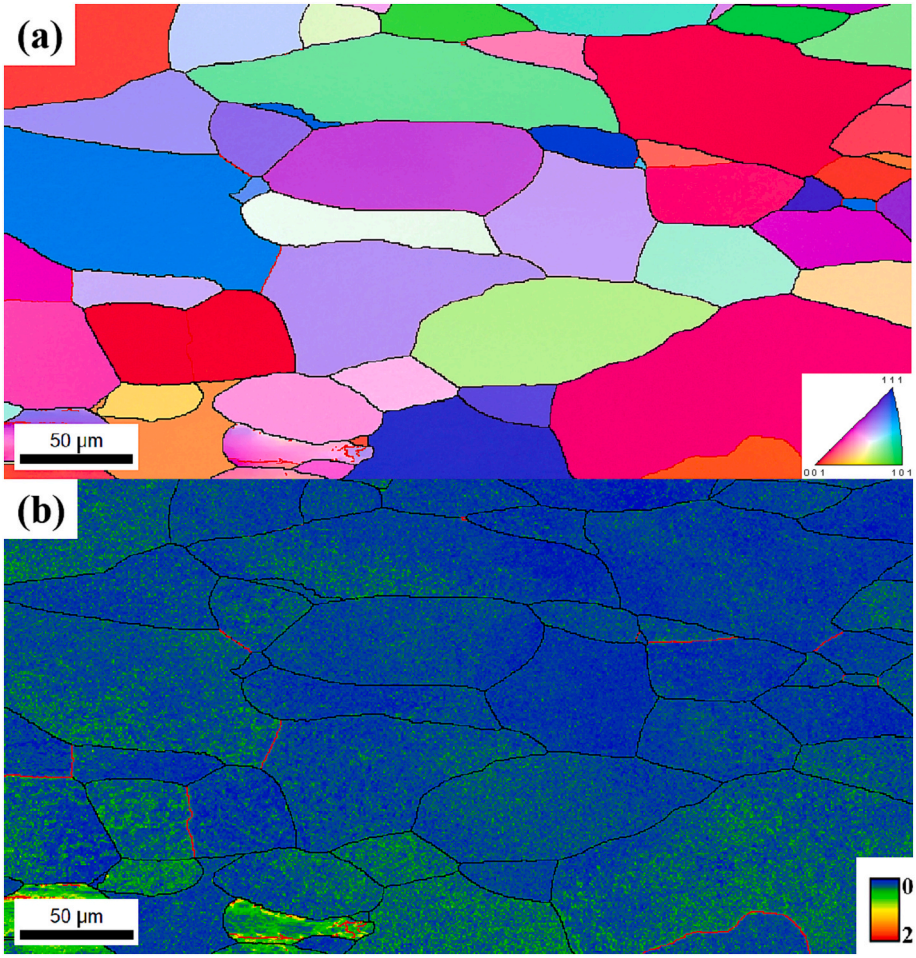

Fig. 1. (a) IPF and (b) KAM maps of course grained Ta. The color legend is shown at bottom right corner and is in degrees for KAM map. The red-colored boundaries are with misorientation angle lying between 2° and 15° and the black-colored boundaries are that >15°. (For interpretation of the references to color in this figure legend, the reader is referred to the web version of this article.)

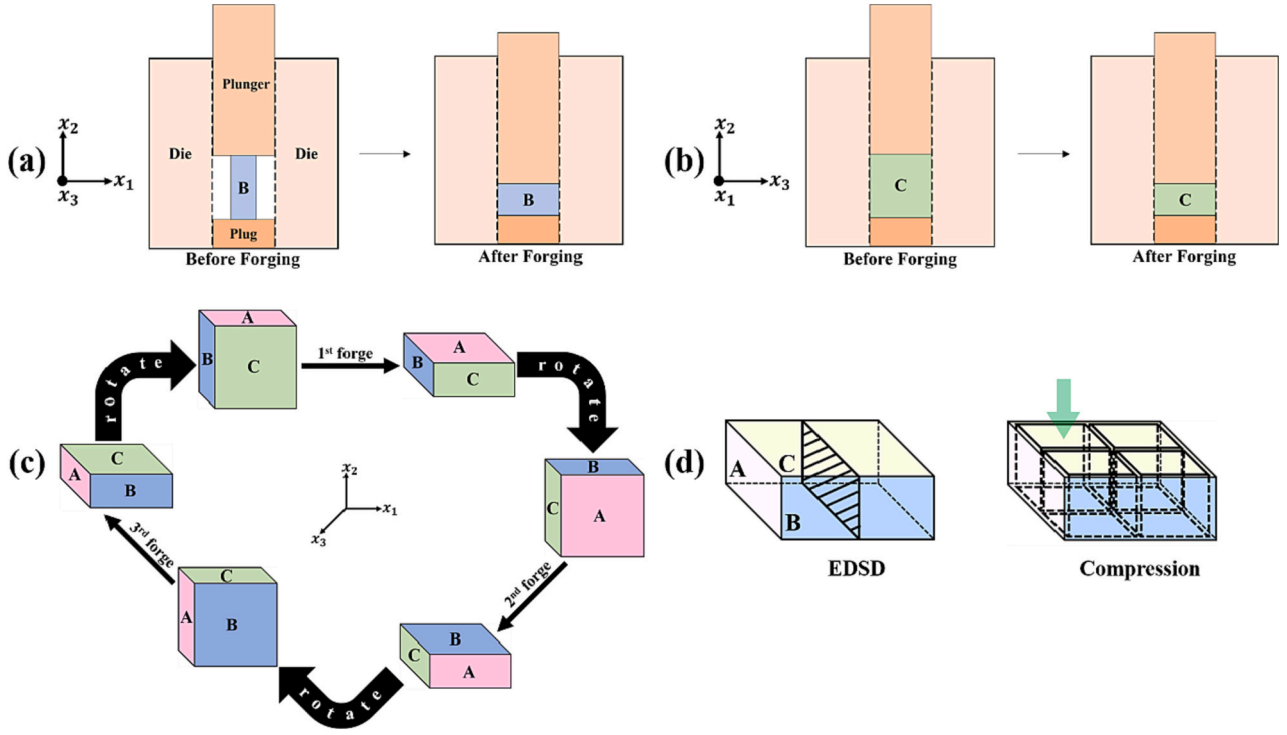

Fig. 2. Schematic illustration of MAF process. The planes perpendicular to the three orthogonal directions are identified as plane **A** (pink), plane **B** (blue), and plane **C** (green). (a) Front and (b) side views of cross-sectioned die block showing sample placed in between the top plunger and bottom plug before and after first forging. (c) Orientation of the sample before and after each forging pass. The sample is rotated after each forging pass. (d) Schematic illustration showing the location on the sample for microstructure and mechanical characterizations. EBSD scans were carried out on the shaded machined part parallel to the plane **A**. Four compression samples were machined out of a forged sample. The arrow shows the direction of the compression axis. (For interpretation of the references to color in this figure legend, the reader is referred to the web version of this article.)

$$\varepsilon_{eff} = \sqrt{\frac{2}{9}\left[(\varepsilon_{11}-\varepsilon_{22})^2+(\varepsilon_{22}-\varepsilon_{33})^2+(\varepsilon_{33}-\varepsilon_{11})^2\right]+\frac{1}{3}(\gamma_{12}^2+\gamma_{23}^2+\gamma_{31}^2)} = \frac{2\,\varepsilon_{11}}{\sqrt{3}} = 0.8. \quad (1)$$

In plane strain compression, $\varepsilon_{11} = -\varepsilon_{22} = \ln 2$ for 50% compression and other strain components in the eq. (1) are zero. Thus, the 3, 6 and 9 passes of MAF accumulated an effective strain of 2.4, 4.8 and 7.2, respectively. The effective strain of the unforged sample is zero. The SPD samples were characterized for their grain size, estimates of ρ, and mechanical properties. The CG Ta rod, 3P, 6P, and 9P samples were characterized through Vickers microhardness, EBSD measurement, and uniaxial compression test. After MAF, the samples were mechanically polished and the Vickers microhardness measured at eight locations on the plane **C** (Fig. 2d) of the sample with 500 g applied load with 10 s dwell time.

2.2. EBSD

EBSD scans were performed parallel to plane A at the end of every 3rd pass as shown in Fig. 2d. The samples were mechanically polished and then electropolished using a mixture of concentrated hydrofluoric acid and sulphuric acid (1:9 by volume) at room temperature for 10 min to remove the residual stress from the surface. EBSD scans were performed on the electropolished surface using ZEISS FEG SEM with 20 kV accelerating voltage and 0.05 μm step size. EBSD scans were analysed using OXFORD HKL and analysis tools for electron and X-ray diffraction (ATEX) software [57].

2.3. Strain rate jump test in compression

Strain rate jump tests were performed in compression at room temperature and at various strain rates ranging from 10^{-4} to 10^{-1} s^{-1} on Zwick UTM using a reversal cage. The dimensions of the compression specimen were 3.8 × 3.6 × 5 mm^3. The compression axis was chosen to be the forging direction at the end of every 3rd pass.

2.4. MD simulations

MD is a versatile computational method to study the behavior of materials at the nanoscale [58–64]. The above sections of this article focused on the modification of grain size, grain boundary character, dislocation density, and texture of Ta subjected to MAF. Complementing these experimental studies, MD can be useful in understanding the evolution of the microstructure at the nano-length scales, such as the formation of defects near HAGBs, pinching and interactions of GBs, and the creation of wavy GBs, and thereby attempting to explain the observed microstructural features.

In the present work, MD simulations were carried out to study the movement, interaction and evolution of GBs using LAMMPS [65]. The list of GBs studied in the current work were used as a supplementary help in formulating the deformation mechanism based on GB motion. Though the range of GB misorientations in MD do not cover that found in Ta polycrystals, the correlations in the structure and behavior of the GBs in both experiments and simulation were found to be comparable. The asymmetric tilt GBs were modeled as shown in Fig. 3a such that there is mobility of dislocations on {110}⟨111⟩ and {112}⟨111⟩ slip systems in the central grain. Simulations were performed on different configurations with the neighboring grains tilted to various angles between 0° and 90°. The simulation box size and number of atoms were selected such that the integer multiples of magnitude of directional

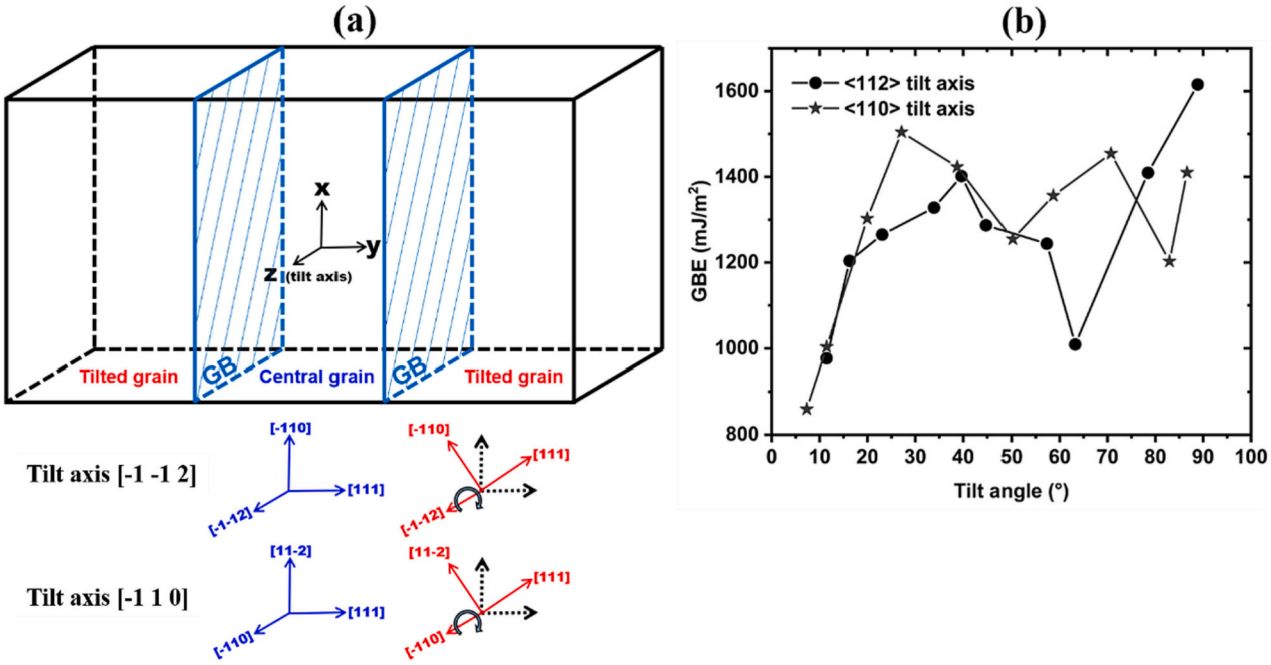

Fig. 3. (a) Schematic illustration of GB configuration. The orientations of the central and tilted grains for two tilt axis configurations are shown at the bottom. The directional vector along y axis for the tilted grains is shown in Table 1 as GB normal. (b) GBE as function of tilt angle.

vectors along *x*, *y*, and *z* axis end at the box edge thus forming periodic boundary. This resulted in different simulation box size and number of atoms for different GB configurations. The GBs were equilibrated using molecular statics simulations. Equilibration of GBs to stable configurations were explained in our earlier works [58,60]. The energy variation as a function of tilt angle as obtained from these calculations are seen in Fig. 3b. The GBE variation as a function of tilt angle for symmetric tilt GBs of Ta can be found in Ref. [66]. Each of the configurations were deformed at a constant engineering shear strain rate of 0.001/ps applied on the *x*-*z* plane in direction of *x* and equilibrated using micro-canonical ensemble, such that the GB move on either $(11\bar{2})$ or $(\bar{1}10)$ and along the [111] direction. The temperature at the start of the simulation was set at 0 K and was allowed to evolve during the deformation. Periodic boundary condition was applied to all directions during deformation. The velocity of GB and shear stress of the configurations were obtained from the simulation. The asymmetric grain boundaries with the direction normal to the GB in the tilted grain (that is, direction along y in the tilted grain) and their corresponding tilt angle and GBE are listed in Table 1. The GBs are referred to by the notation $\langle tiltaxis\rangle/\theta^{\circ}$ representing the tilt axis and misorientation angle. Potential developed by Y. Chen et al. [67] was used in the current simulations as the predicted the lattice constant, cohesive energy, elastic constants and core structure of screw dislocation in bulk Ta close to experimental and first principles data.

Table 1
Asymmetric grain boundaries and their GBEs. GB normal refers to the direction normal to the GB (direction along y) in the tilted grain.

Tilt axis ⟨110⟩		Tilt axis ⟨112⟩	
GB	GBE (mJ/m^2)	GB	GBE (mJ/m^2)
⟨4 4 3⟩/8°	860	⟨20 12 16⟩/11°	977
⟨8 8 5⟩/11°	1003	⟨35 71 53⟩/16°	1204
⟨26 26 10⟩/19°	1303	⟨11 35 23⟩/23°	1265
⟨23 23 5⟩/27°	1505	⟨5 53 29 ⟩/33°	1328
⟨1 1 5⟩/38°	1423	⟨0 16 8⟩/39°	1402
⟨−26 − 26 10⟩/50°	1255	⟨−2 22 10⟩/44°	1287
⟨−1 − 1 19⟩/58°	1356	⟨−17 55 19⟩/57°	1244
⟨1 1 − 1⟩/70°	1454	⟨−14 34 10⟩/63°	1009
⟨−11 − 11 29⟩/82°	1203	⟨−10 14 2⟩/78°	1410
⟨−13 − 13 23⟩/86°	1410	⟨−59 61 1⟩/88°	1616

3. Results

3.1. Flow stress during MAF

The true flow stress was calculated using the force recorded during forging (F), initial area facing the plunger (A_0), and the plastic strain (e_{22}) as $(F/A_0) \times (1 - e_{22})$. The force increased rapidly as soon as the sample filled the die. The true flow stress of Ta samples as a function of accumulated equivalent strain during each pass is shown in Fig. 4a. The transparent blue colored band represent the locus of flow stress during each pass. The flow stress increased significantly between the first and second passes. After the second pass, the flow stress increased gradually till the 9th pass.

3.2. Vickers microhardness

The average values of the Vickers microhardness measured at eight locations in each specimen is shown with error bars in Fig. 4b. The microhardness values increased significantly from CG to sample after 6th pass. The mean value of microhardness decreased between the 6P and 9P samples, however, with high scatter in 9P. The scatter in hardness values showed that the variation in the microhardness values measured at multiple locations of a sample was minimum in the CG specimen and increased with number of passes.

3.3. Microstructure

Band contrast (BC) images with low angle grain boundaries (LAGBs) and HAGBs are shown in Fig. 5. LAGBs are those with misorientation angle between 2° and 15° and HAGBs are those with misorientation angle >15°. It was seen that increase in the number of passes refined the microstructure. 3P sample showed inhomogeneous microstructure with both small and large grains. The larger grains had sub-grains within them (the presence of LAGBs) suggesting that the refinement of microstructure is in process. With increase in the passes the number of larger

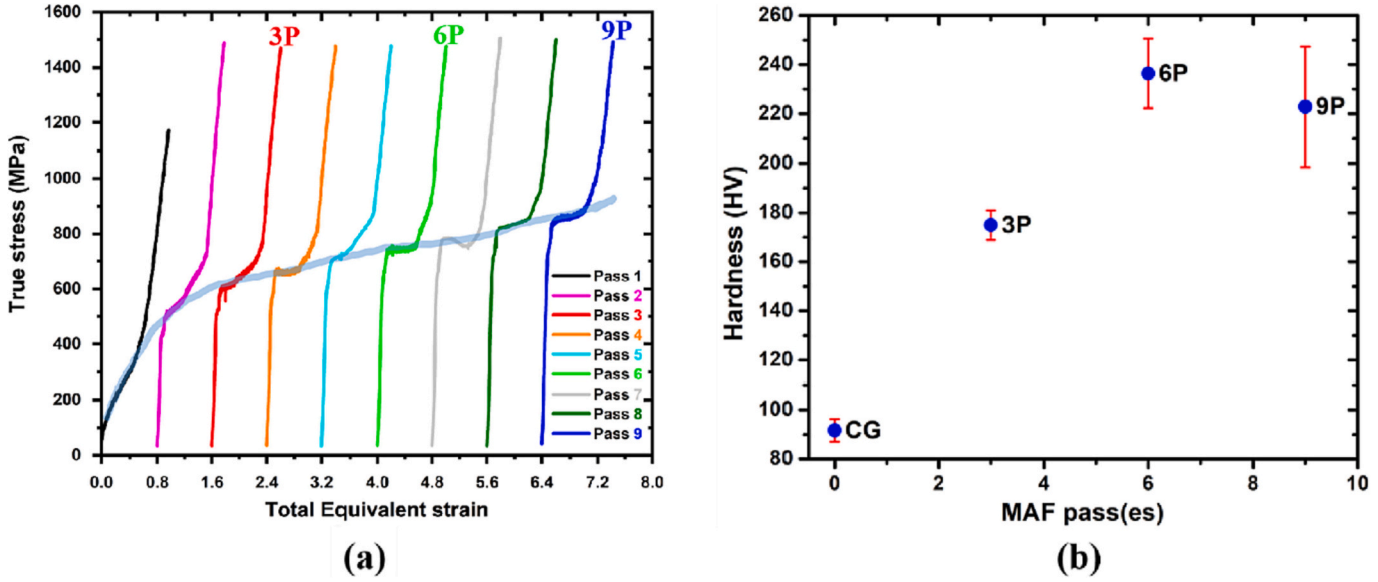

Fig. 4. (a) Flow curve during MAF of Ta as a function of equivalent strain accumulated after each pass. Each color represents the flow stress during each pass. The transparent blue colored band represent locus of flow stress during each pass. The labels 3P, 6P, and 9P on the flow curve represent the samples that were characterized for their microstructural and mechanical properties. (b) Vickers microhardness values of CG, 3P, 6P, and 9P samples. The error bars represent the scatter due to multiple indents at various locations on the **C** plane (Fig. 2d). (For interpretation of the references to color in this figure legend, the reader is referred to the web version of this article.)

grains decreased and the smaller grains increased. 9P microstructure had fewer sub-grains within UFGs as compared to earlier pass samples. The misorientation angles above 2° were considered as boundaries (either LAGB or HAGB) and those below 2° were taken as in-grain misorientations and analysed using grain average misorientation (GAM), KAM, and grain orientation spread (GOS), their maps are shown in Fig. 5. KAM is the in-grain misorientation calculated as the average of the misorientation angles measured between neighboring points, but excluding neighbors with misorientation angle >2°, i.e. sub-GBs within the grains are excluded in the KAM calculation.

The microstructural features in Fig. 5 that are relevant for further explanation of texture and mobility of GBs are cropped and shown in Fig. 6. Fig. 6a shows a grain having a gradient of TF values i.e. color gradient change between yellow and red. This gradient of TF values can be correlated to on-going deformation process of the larger grain. A similar observation can be seen in 6P sample in Fig. 6b. Fig. 6c and d represent 3P sample where small recrystallized grains were found surrounding a large hard grain (high TF value - red color). The arrows point out the recrystallized grains having blue color (low GOS value). In Fig. 6e, 3P sample was found to have wavy LAGB within a grain (as shown by arrows). Fig. 6f shows the KAM map of 6P where LAGBs or nucleating group of dislocations from a HAGB show high KAM value (green-yellow colors). Fig. 6g shows the bands of LAGBs aligned parallel to each other within the HAGBs forming a micro-shear band (MSB). The inside plot shows the point to point misorientation in the MSB region.

MAF changed the grain size, fraction of high angle boundaries f_{hagb}, fraction of LAGBs ($f_{lagb} = 1 - f_{hagb}$), and fraction of coincidence site lattice (CSL) GBs (f_{csl}). The cumulative frequency distribution of grain diameter considering both LAGBs and HAGBs is shown in Fig. 7a. CG sample had the largest grains due to its annealed microstructure. 3P sample had few large grains and many small grains, making the distribution move to lower grain size values. In the 6P and 9P samples the fraction of large grains reduced further making their grain size distribution shift to even lower values. 9P sample showed the lowest grain size distribution. While after 3 passes, the microstructure showed bimodal grain size distribution, at the end of 9 passes, the microstructure showed uniform grain size distribution. The average grain diameter was in the order: CG - 64.02 μm > 3P - 4.04 μm > 6P - 1.43 μm > 9P - 0.76 μm. It can be seen that the grain diameter decreased significantly between CG and 3P samples. The cumulative frequency distribution of grain size considering only HAGBs is shown in Fig. 7b. The grain size distribution with and without sub-grains (Fig. 7a and Fig. 7b, respectively) was similar. The average grain diameter when only HAGBs were considered was in the order: CG - 76.45 μm > 3P - 27.69 μm > 6P - 11.18 μm > 9P - 3.52 μm. The fraction of high angle boundaries f_{hagb} can be estimated from the cumulative frequency distribution of misorientation angle plot (Fig. 7c) by considering the fraction above 15° misorientation. f_{hagb} was found to be in the order: CG - 0.898 > 9P - 0.53 > 6P - 0.36 > 3P - 0.321. Of the MAF samples, 9P sample had the highest f_{hagb}. As fragmentation of grains during initial stage of deformation generated sub-grains, the 3P and 6P samples had large fraction of sub-grains within grains and thus had a lower f_{hagb}. Increase in the passes to 9P, increased the f_{hagb} indicating the transformation of sub-grains to HAGBs. The variation of number fraction of LAGBs, HAGBs, and CSL is shown as bar chart in Fig. 7d. With increase in passes, the LAGBs decreased while HAGBs and CSL increased. The fraction of CSL is relatively lower than both the LAGBs and HAGBs.

The high value of KAM within grains are due to the high in-grain misorientations arising from the strain field of geometrically necessary dislocations (GNDs) generated during plastic deformation in each forging pass. The cumulative distribution of KAM is shown in Fig. 8. The distribution was lowest for the CG sample and increased for the forged samples, attributed to the accumulation of GNDs. The average KAM ($\overline{\varphi}_{loc}$) of the microstructure can be used to estimate the GND density (ρ_{GND}) as,

$$\rho_{GND} \approx \frac{1}{b}\frac{\left(\overline{\varphi}_{loc} - \overline{\varphi}_{loc,err}\right)}{\Delta x}, \tag{2}$$

where b is the magnitude of Burgers vector = 0.28629 nm, Δx is the step size = 0.05 μm. $\overline{\varphi}_{loc,err}$ is the error in the calculation of local misorientation and can be assumed to be ≈ 0.1° [17,68] such that CG sample had ρ of 10^{12} m^{-2}. The calculated ρ_{GND} is found to be in the order: 6P - 12 × 10^{13} m^{-2} > 3P - 11.5 × 10^{13} m^{-2} > 9P - 11.2 × 10^{13} m^{-2}. The average KAM of each sample is plotted as a function of f_{hagb} in Fig. 8. The change in the KAM values can be attributed to the transformation of GNDs and LAGBs to HAGBs.

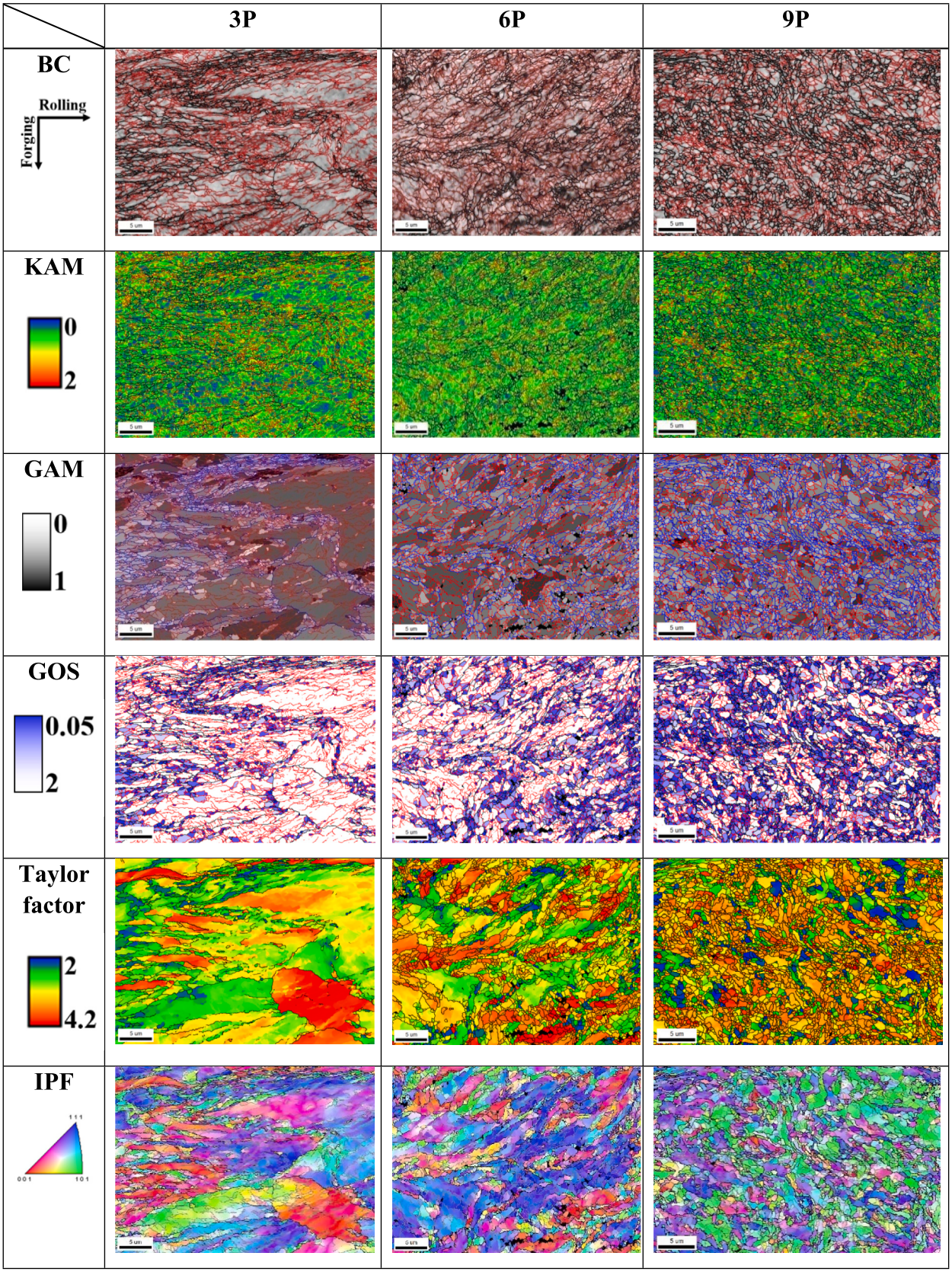

Fig. 5. Band contrast images, KAM, GAM, GOS, TF, IPF maps overlaid with GBs of 3P, 6P and 9P samples. The red-colored boundaries are with misorientation angle lying between 2° and 15° and the black-colored boundaries are that >15°. For better visualization, the boundaries with misorientation angle lying between 2° and 15° in IPF map are shown in grey color. In TF map, boundaries with misorientation angle >15° are shown. The color legend of each map is shown in the left most column. (For interpretation of the references to color in this figure legend, the reader is referred to the web version of this article.)

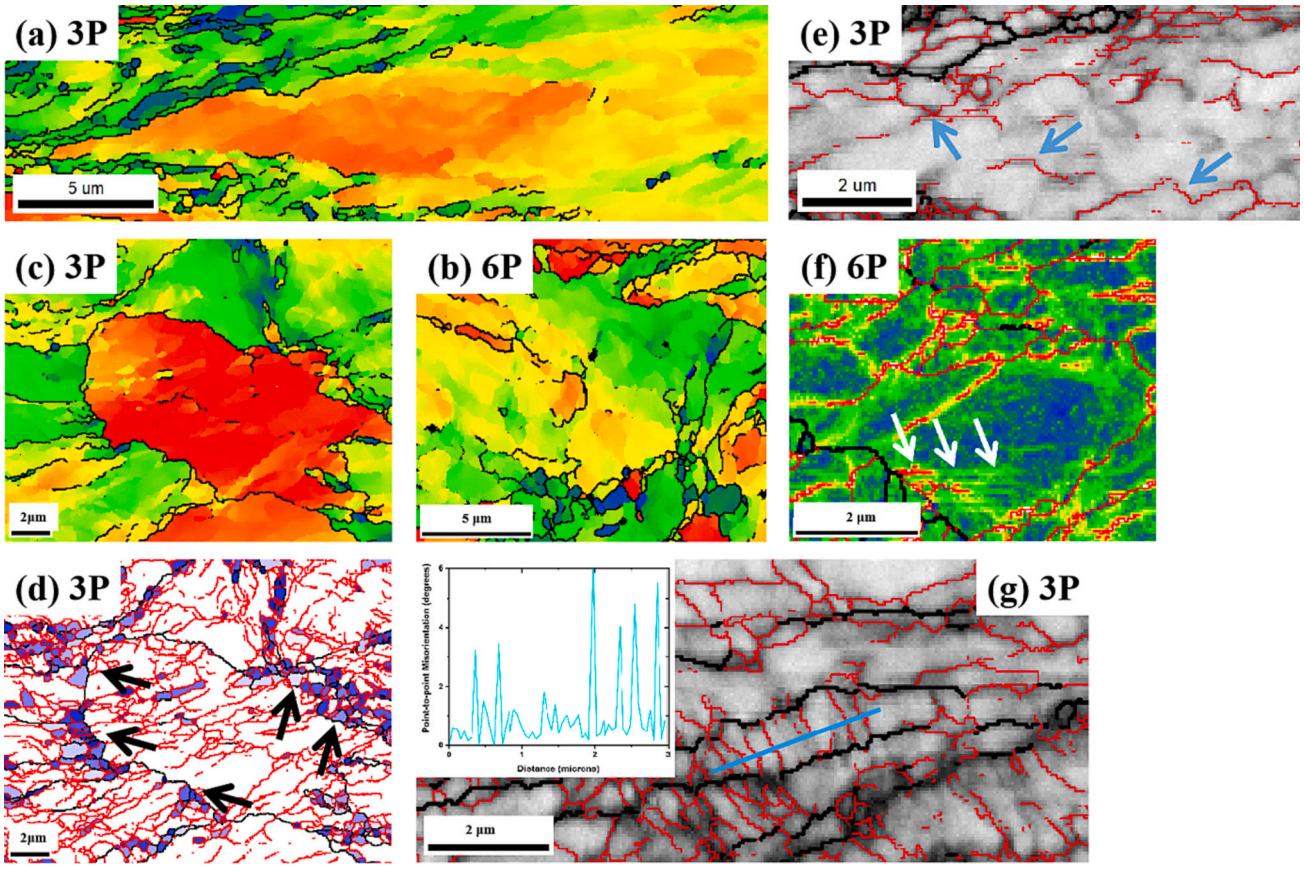

Fig. 6. Gradient of Taylor factor values within grains of (a) 3P and (b) 6P samples. (c) TF and (d) GOS maps of softer recrystallized grains (low TF) along the boundaries of harder grains (high TF) in 3P. (e) Wavy structure of LAGBs in 3P. (f) High value of KAM near the GB nucleating dislocations. (g) Micro-shear bands (MSBs) in 3P. Inset shows the point to point misorientation in the MSB region. The scales and coloring of the boundaries are similar to that in the Fig. 5.

GAM is the average of misorientation between neighboring points within a grain where the grain is designated with a boundary having misorientation >15°. GAM values mapped on each grain for each sample is shown in Fig. 5. The color legend represented by the white-colored grains have zero or low GAM values and the dark-colored grains represent high GAM values. GAM can be attributed to deformation and the generation of GNDs within grains. The 3P sample had grains with both low (light colored) and high (dark colored) values of GAM. It was seen that grains with low GAM increased with increase in passes (see Fig. 8) signifying an increase in grains having low dislocation density. The GAM distribution (Fig. 8) was lowest for the CG sample and increased after initial 3 passes signifying accumulation of GNDs within the large grains of the 3P sample. The distribution shifted to lower values for 6P and further for 9P suggesting a decrease in the GNDs with increasing passes. Fig. 8 showed that GAM is inversely related to f_{hagb}, suggesting that the reduction of sub-grain boundaries (increase in f_{hagb}) is related to a reduction in ρ.

Grain orientation spread (GOS) is the average value of the deviation of each orientation point in the grain (having HAGBs of 15°) with the average orientation of the grain. Each grain is assigned one GOS value. Grains with GOS value <2° are considered as recrystallized grains [69]. GOS values mapped on each grain for each sample is shown in Fig. 5. Higher values of GOS imply higher gradients of orientation and are linked to higher GNDs. From Fig. 8 CG sample had the highest fraction of grains with GOS < 2° ($f_{GOS<2^\circ}$) of 0.99, signifying a high fraction of recrystallized grains. 3P sample showed localized recrystallized grains surrounded by deformed grains with sub-grain structures. As read from Fig. 8 $f_{GOS<2^\circ}$ for 3P, 6P, and 9P samples were found to be 0.34, 0.52, and 0.70, respectively. $f_{GOS<2^\circ}$ increased from 3P to 9P samples with increase in fine recrystallized grains. The distributions increased from CG to 3P and then decreased from 3P to 9P (Fig. 8). The shifting of GOS distribution to lower angles with increase in passes from 3 to 9 showed that the ρ and sub-grains within grains decreased.

Taylor factor [70] was calculated using plane strain deformation gradient tensor, and with the assumption of same critical resolved shear stress on {110}, {112}, and {123} slip planes. Higher value of Taylor factor represents grains hard to deform, whereas lower values represent soft grains. The average Taylor factor was found to be 3.18 for CG, 3.21 for 3P, 3.20 for 6P, and 3.21 for 9P. In Fig. 6a and b, 3P and 6P samples showed gradients of TF values within grains which suggesting that with increase in passes, the larger grains undergo deformation to form sub-grains and finally recrystallize as small grains. From Fig. 6c and d, it is seen that the softer grains in 3P were predominantly recrystallized grains along the boundaries of harder grains.

3.4. Texture evolution

The texture evolution during MAF was evaluated using orientation imaging microscopy through EBSD. This was represented using Euler angles φ_1, Φ, and φ_2 in the Euler space to study the textural evolution of deformed samples. For plane strain conditions, the typical textural fibers observed in BCC are α (⟨110⟩ ∥ *RD*), γ (⟨111⟩ ∥ *ND*), η (⟨001⟩ ∥ *RD*), and ε (⟨110⟩ ∥ *TD*), where RD, ND, and TD represent rolling, normal and transverse directions, respectively. Orientation distribution function (ODF) sections at $\varphi_2 = 0^\circ$ and $\varphi_2 = 45^\circ$ are shown in Fig. 9a and 9b. Fibers can be visualized by the key fig. [71] shown in Fig. 9c. Texture components of $(110)[1\bar{1}0]$ and $(111)[0\bar{1}1]$ developed after 3 passes. As γ fiber grains can accommodate higher density of dislocations, grains with this texture nucleated throughout the recrystallization and deformation processes [72]. After 9th pass, the $(111)[1\bar{1}0]$ component of α fiber and

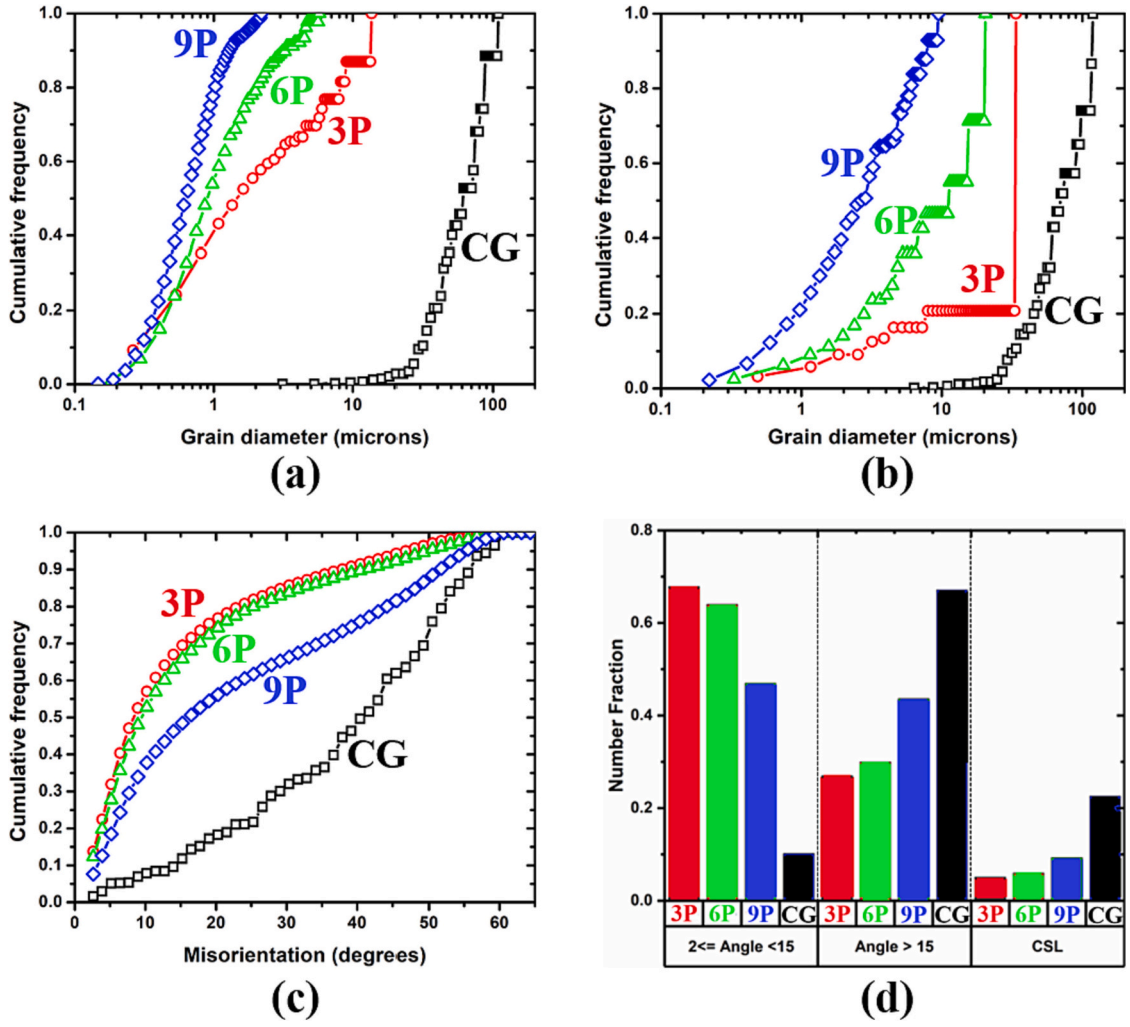

Fig. 7. Cumulative frequency distribution of (a) grain diameter including grains with both LAGBs and HAGBs, (b) grain diameter of grains with only HAGBs, and (c) misorientation angle from 2° to 65°. (d) Number fraction of LAGBs (misorientation angle between 2° and 15°), HAGBs (misorientation angle >15°), and CSL GBs of CG, 3P, 6P, and 9P samples.

the $(111)[0\bar{1}1]$ component of γ fiber were dominant.

Texture fiber plots are shown in Fig. 10 and major fiber components are listed in Table 2. A value greater than one signifies the prominence of a particular fiber. Grains were partitioned with criteria of GOS < 2° called here as 'recrystallized', and with GOS > 2° referred to as 'deformed'. Texture for each of the 'recrystallized', 'deformed' as well as all the grain referred to as 'combined' were determined (Table 2 and Fig. 10). Two observations were made from Fig. 10 – one, the combined fiber density after each pass, and second, the fiber difference in deformed and recrystallized grains.

For 3P and 6P the fiber of the deformed part and all grains combined part were similar, while the recrystallized grains showed a different fiber. For 9P the recrystallized texture was similar to the deformed and complete texture, but with lower fiber density. The fibers in recrystallized grains evolved from η and ε in 3P, to α and η in 6P and finally to α, γ and ε fibers in 9P. The fibers in deformed grains evolved from α and ε in 3P to α in 6P and finally as α, γ and ε fibers in 9P. From this it can be inferred that the consumption of deformed grains by recrystallization process and the consumption of recrystallized grains by deformation process happen simultaneously. In an earlier work [73] the γ fiber was reported to nucleate first due to recrystallization process, however in the current studies η and ε fibers were first nucleated in 3P. This can be attributed to the nucleation of η and ε fibers along GBs of harder grains (higher TF) (Fig. 6c TF and 6d GOS). The strain-induced boundary migration (SIBM) of LAGBs can be the reason for nucleation of γ fibers which will be discussed in later sections.

3.5. Flow behavior and strain rate sensitivity

The true stress-true strain flow curves obtained in compression during which strain rate jumps were also carried out as shown in Fig. 11a. The yield stress of CG, 3P, 6P, and 9P samples were found be 178, 465, 613, and 653 MPa, respectively, showing that the yield stress increased with increase in passes. The 9P showed a low strain hardening rate as compared to the other passes. The strain rate sensitivity ($m = \Delta ln\sigma/\Delta ln\dot{\varepsilon}$) of CG, 3P, 6P, and 9P samples determined using strain rate jump test were 0.039, 0.015, 0.012 and 0.013, respectively and their corresponding stress exponents ($n = 1/m$) were 26, 65, 81, and 78, respectively. m decreased from CG to 6P, with 9P being similar to 6P. The increase in f_{hagb} in 9P sample could be responsible for strain rate sensitivity not decreasing further [18]. The apparent activation volume (V_a) was calculated using Taylor factor (M), Boltzman constant (k), test temperature (T), and strain rates ($\dot{\varepsilon}$) and stresses (σ) between strain rate jump test using,

$$V_a = MkT\frac{ln\left(\dot{\varepsilon}_2/\dot{\varepsilon}_1\right)}{\sigma_2 - \sigma_1} \quad (3)$$

From Fig. 11b, the activation volume was seen to decrease with stress

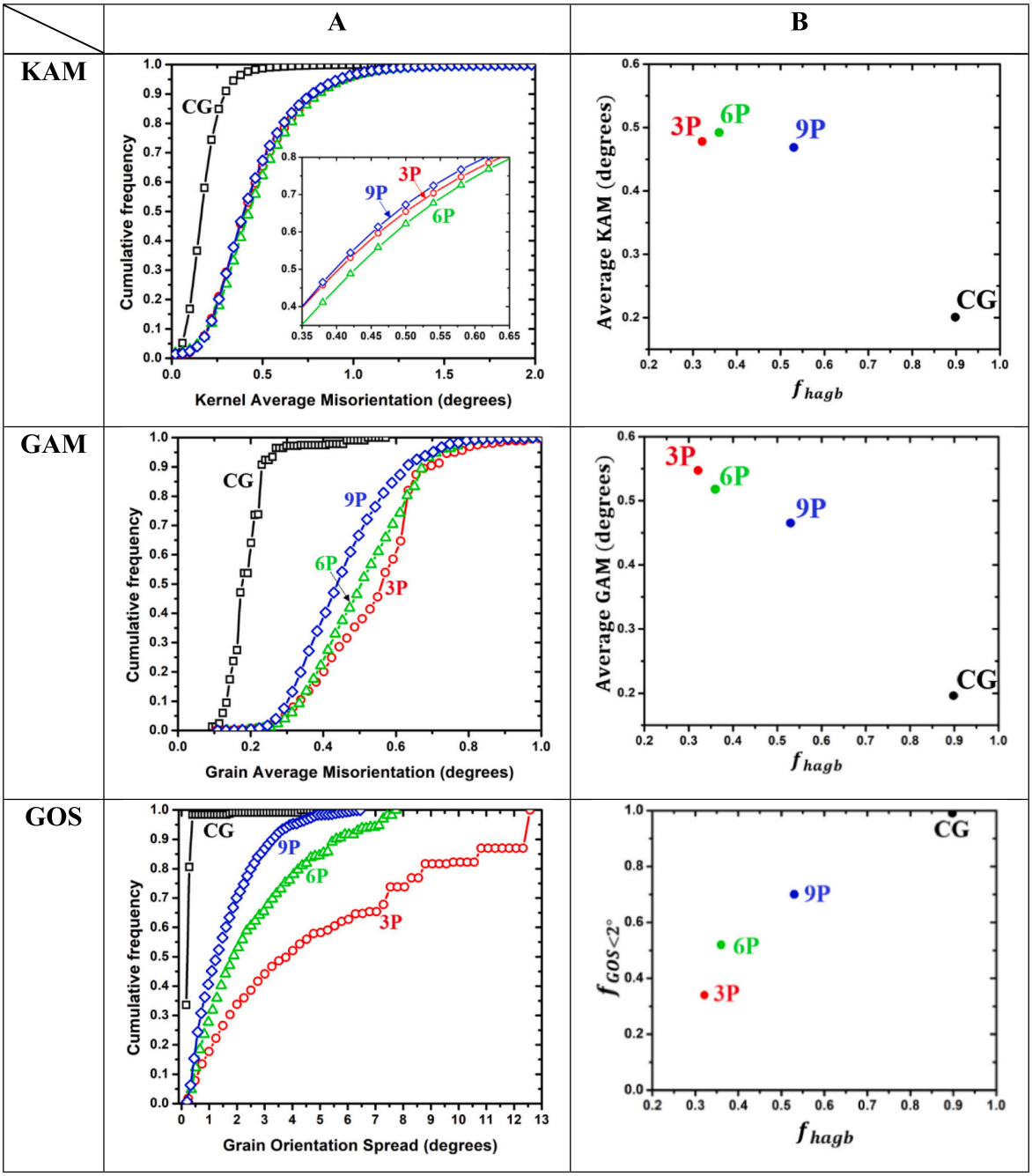

Fig. 8. Cumulative frequency distribution of KAM, GAM and GOS are shown in A column. Average KAM, average GAM and $f_{GOS<2^\circ}$ as a function of f_{hagb} for each sample are shown in B column. The labels and colors represent the different samples.

as is expected in a thermally activated deformation.

3.6. Interaction of GBs: MD simulations

The refinement of grains using SPD can have several mechanisms such as pinching of GBs [74], shear band formation [75], dislocations forming sub-structures [30] and sequentially forming HAGBs [17,51]. MD simulations were performed to see if the above-mentioned mechanisms of interactions of LAGBs, HAGBs, and dislocations take place. The MD results of all GB configurations and their relevant experimental observations are listed in Table S1 in the supplementary file. The atoms in the MD snapshots were colored based on the common neighbor analysis (CNA). Atoms with eight neighbors are blue colored and atoms with more or less than eight neighbors are red colored. The interactions of the GBs are attached as supplementary videos with their file names as "tilt axis_misorientation angle". GB configurations categorized as LAGB, dissociating HAGB, HAGB with ledges, and mobile HAGB are shown as snapshots during their interactions in Fig. 12. The dislocations are characterized using dislocation extraction algorithm (DXA) in OVITO [76]. MD simulation results have two parts - mobility of GBs and their interactions.

3.6.1. Mobility of GB

The collective motion of dislocations as individual entities in LAGBs (as in ⟨112⟩/11° and ⟨110⟩/8° configurations) is possible because individual dislocations are sufficiently spaced and do not interact with each other. This collective motion of dislocations in LAGBs have also been observed earlier [77]. As the GB θ increases from 8° to 16°, the

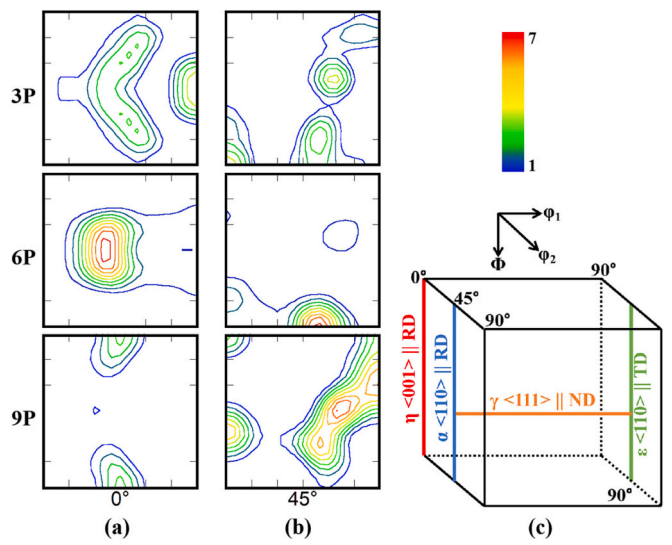

Fig. 9. (a) and (b) are sections of ODF at $\varphi_2 = 0°$ and $\varphi_2 = 45°$, respectively for 3P, 6P, and 9P samples. The color legend is shown on the right side of the ODF. (c) is the key figure for BCC texture fibers.

dislocation spacing in the boundary decreases. Thus, the forces between the neighboring dislocations leads to dislocation reactions that result in the formation of sessile dislocations as seen in ⟨112⟩/16°. This leads to the formation of wavy LAGBs. Such wavy LAGBs were experimentally seen in 3P sample (Fig. 6e).

The motion of HAGB involved development of disconnections and ledges on it, which contributes to change in the PE of the system. Change in PE of the system have been attributed to the changes in GB structure [78]. A ledge is a step in the GB out of GB plane, whereas a disconnection is a step and a dislocation [79,80]. The high stored energy in HAGB was dissipated by the nucleation of dislocations from disconnections and ledges. The high value of KAM near the GB region in the experimental results can be attributed to nucleated dislocations near GBs (Fig. 6f). Motion of disconnections and ledges help the GBs to move [81,82]. The

Table 2
Texture fibers for combined, recrystallized, and deformed grains in each of the passes.

	Combined	Recrystallized	Deformed
3P	α and ε	η and ε	α and ε
6P	α	α and η	α
9P	α, γ, and ε	α, γ, and ε	α, γ, and ε

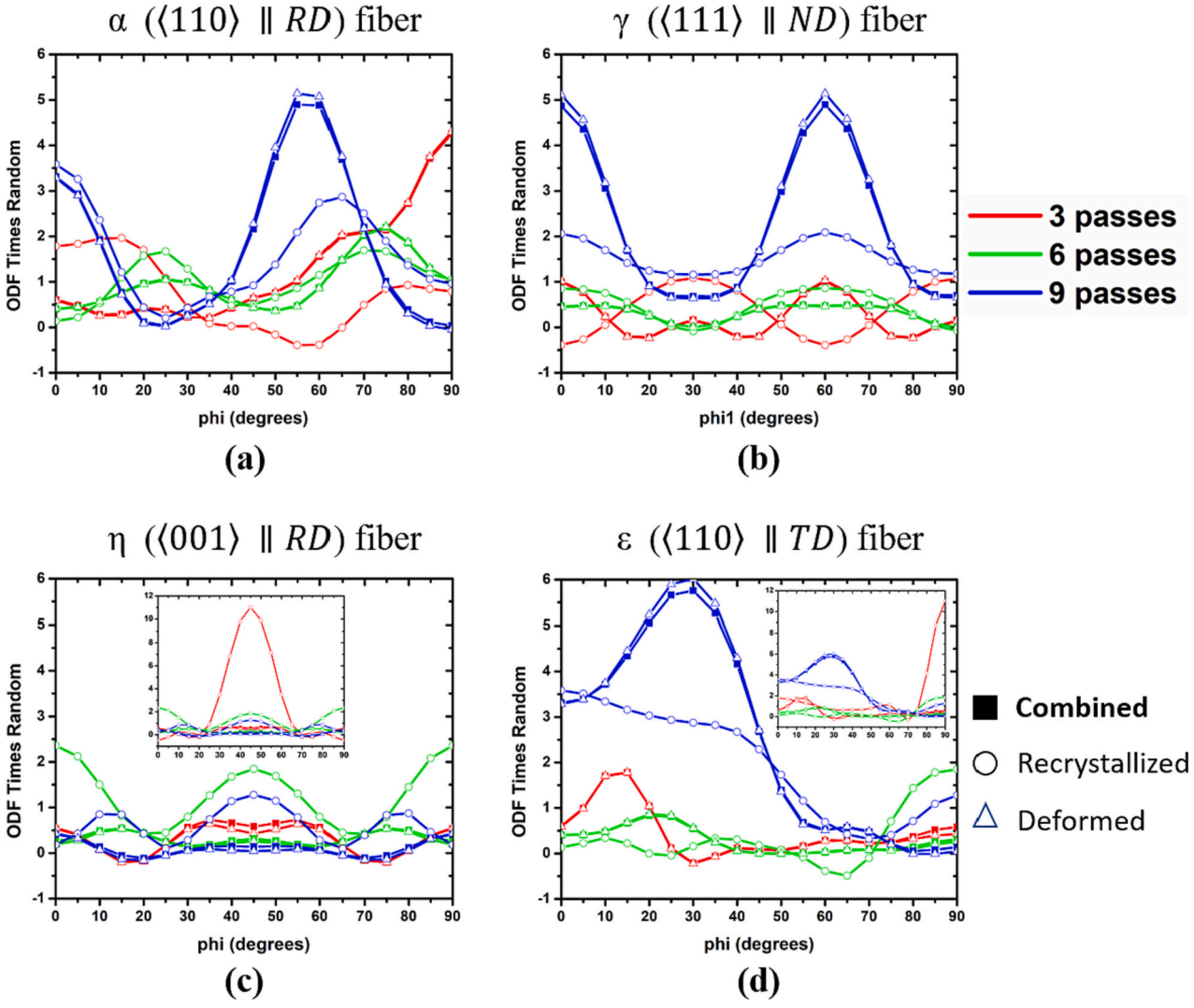

Fig. 10. Distribution of α, γ, η and ε fibers for recrystallized, deformed, and all the grains. The inset plot is with data points of recrystallized grains of 3P samples. It is separated from the main plot to scale in a similar range.

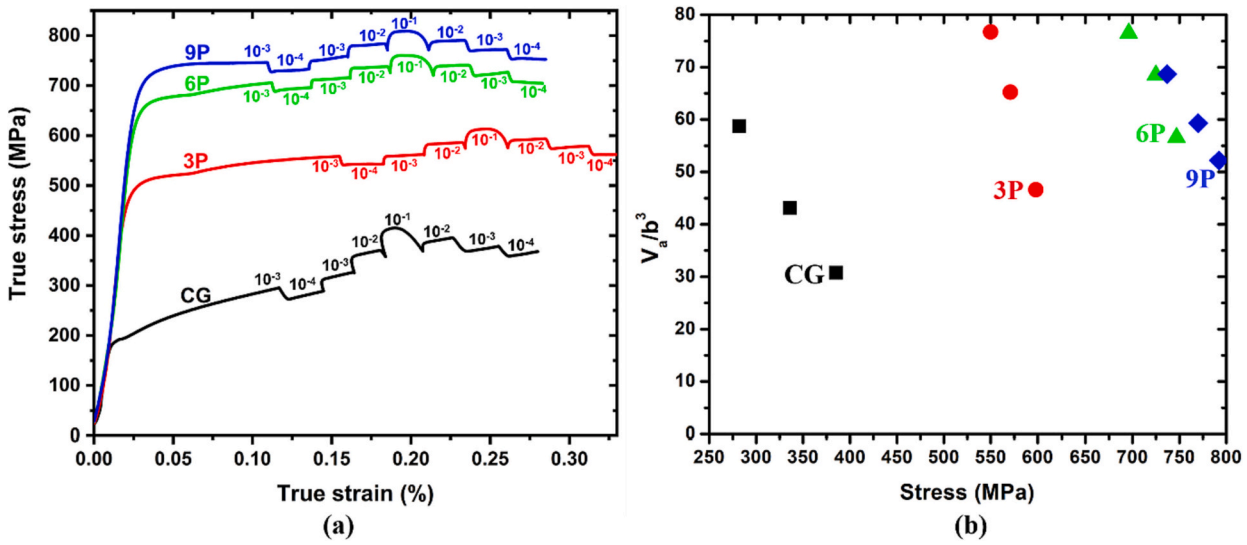

Fig. 11. (a) shows the true stress-true strain plots in compression with strain rate change test at various strain rates (shown in unit of s^{-1}) represented along the flow curve. (b) shows the apparent activation volume normalized with b^3 as a function of stress.

combined movement of dislocation and ledges together led to the movement of HAGB as in ⟨110⟩/50 °, 83 °, 86°. The ⟨112⟩/23 °, ⟨110⟩/27° HAGBs consist of different types of dislocations closely packed in the GB region. With the application of stress, an array of dislocations equivalent to a LAGB nucleated from these HAGBs. The simulations showed that these HAGBs dissociated into two LAGB (see Fig. 12 ⟨112⟩/23°), one of which was mobile and migrated away from the boundary, and the other LAGB that was left behind again dissociated to form glissile dislocations. The HAGB configuration ⟨110⟩/20° dissociated directly to form mobile LAGBs. The sudden decrease in PE/atom value (shown in Fig. S1 in the supplementary file) can be attributed to the energetically feasible dissociation of the high energy HAGB to low energy LAGBs. The distance between the ledges increased for HAGB with higher θ, leading to a smaller number of nucleating dislocations from the GB. This can be attributed to the repetitive structural units[1] in the HAGBs, which when moved out of the GB plane formed ledges and disconnections. Bobylev et al. [83] pointed out the structural units in the HAGBs and their significance in GB mobility. The position of the structural units, their numbers and repetitiveness in the GB plane, controls the dislocation nucleation or GB thickening (in case of immobile GB).

If the structural units repeat alternatively, then the nucleation of an array of dislocations from GB can be observed [83]. If the structural units are continuous, then the amount of nucleation of dislocations is reduced which lead to dissociation of HAGB into LAGB and HAGB. So, the pristine ⟨112⟩/33° HAGB dissociated into LAGB and HAGB with comparatively less drop in PE than ⟨112⟩/23°. For HAGB with higher θ, the GB became very close to immobile configuration (⟨112⟩/39 °, 44 °, 78 °, 88 °, ⟨110⟩/39 °, 70°).

3.6.2. *Interaction of GB*

The wavy structure of LAGBs is associated with a local radius of curvature which can act as nucleation sites for dislocations, as was seen in ⟨110⟩/11°. The annihilation of GBD in ⟨112⟩/11 °, 16° and ⟨110⟩/8° configurations created a low dislocation density configuration and in ⟨110⟩/11° point defects increased after annihilation of dislocations. The continuous nucleation of dislocations from ⟨110⟩/58° HAGBs led to movement of ledges away from GB plane, allowing the HAGBs to interact. While in case of ⟨112⟩/57 °, 63° HAGBs the interaction is due to the nucleated dislocations from the ledges. The interaction between the nucleated dislocations increases ρ and point defects. The interaction of the wavy LAGBs and HAGBs can result in pinching of wavy GBs. The newer boundaries thus created resulted in the formation of the sub-structure. The dislocations emitting from HAGBs (⟨110⟩/83°, ⟨112⟩/63°) formed shear bands which can be attributed to the MSB in 3P sample (Fig. 6g) and also observed during rolling of Ta [84–86]. The relevance of GB migration and recrystallization can be found in reference [53, 73]. The SIBM of GBs favored bulging, pinching of GBs and subsequently forming a recrystallized grains [73].

The reduced mobility of HAGBs as compared with LAGBs can be correlated to the recrystallization process of fiber texture. The higher mobility of LAGBs led to their interaction earlier as compared to that of HAGBs. γ fiber was reported to have formed from regions of high dislocation density [73]. The formation of sub-structures by dislocations and the interaction of LAGBs led to the consumption of these dislocations to form recrystallized grains with γ fiber. It can thus be inferred that the main reason for the recrystallized grains to have γ fiber is because of the high mobility of LAGBs.

4. Discussion

This work demonstrated that Ta could be subjected to SPD through the process of MAF. This resulted in a refinement of the microstructure to sub-micron levels and an increase in the hardness and flow stress, that can be attributed to the increase in the ρ and a decrease in grain size. The grain size distribution and ρ were characterized using EBSD analysis. Earlier work using the Modified Estrin–Toth–Molinari–Brechet constitutive model for SPD of Ta has shown a saturation of flow stress and a slight decrease in ρ after an effective strain of 4 [87]. As GBs act as barriers to dislocation motion, a reduced grain size increases the strength, according to the Hall-Petch relation. Apart from the grain size effect, the variation in strength between the MAF samples would also depend on the f_{hagb}, boundary density, grain size, and texture. 3P and 6P showed similar misorientation distributions (Fig. 7c), but different grain size and texture (Fig. 7a, b and Fig. 9), thereby resulting in different strength. The increase in the strength of the 9P sample was due to the ultra-fine grains. The MAF Ta showed a saturated flow stress in compression test, as compared to CG Ta that showed considerable work-hardening. Wei et al. [88] obtained a strain rate sensitivity of 0.060 and 0.025 for unprocessed and ECAE Ta (after ε_{eff} of 4.64), respectively. They reduced the average grain diameter of Ta from 20 μm to 200 nm.

[1] Structural units are periodically arranged atomic clusters in the GB [83].

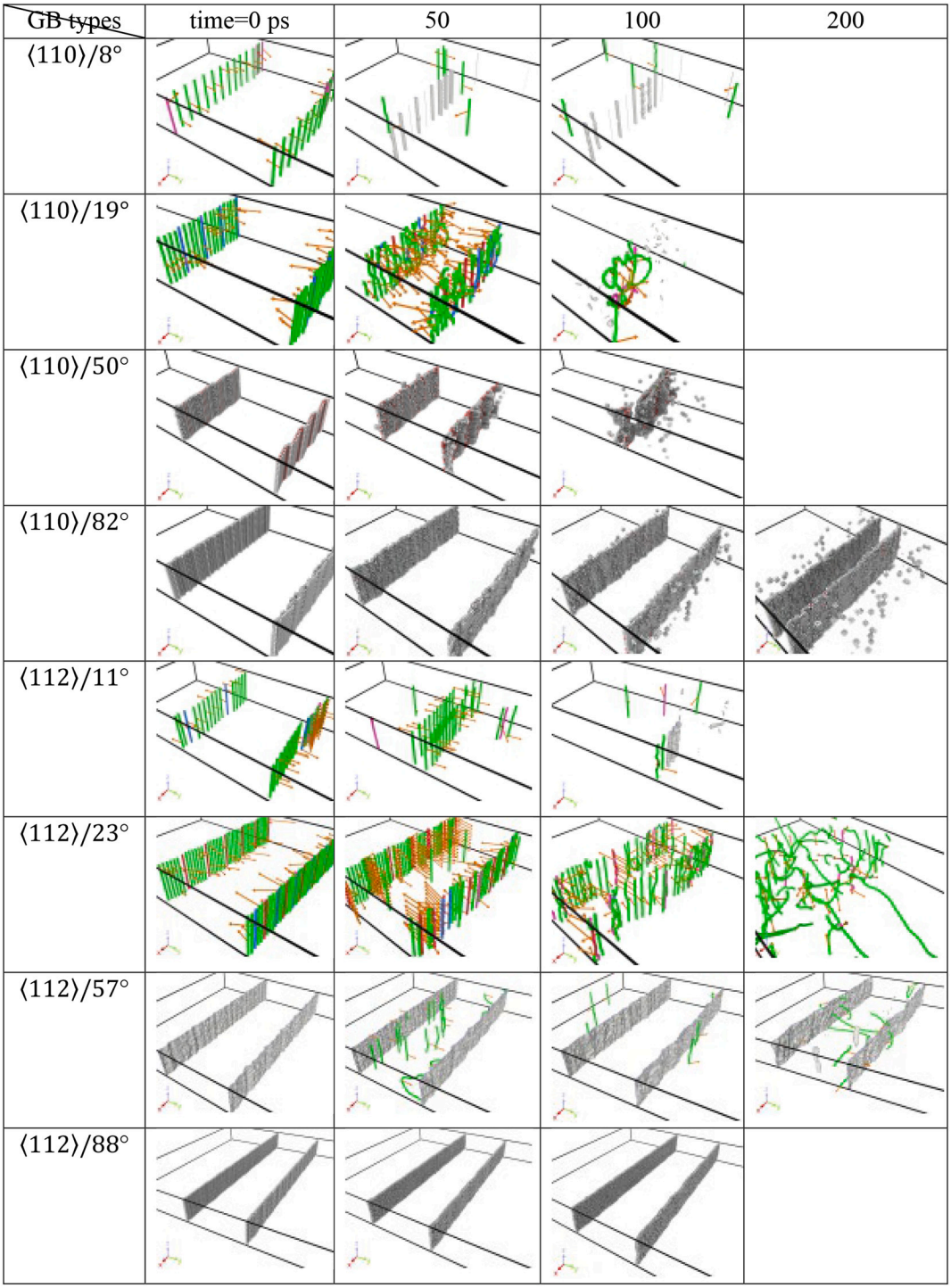

Fig. 12. Snapshots of MD simulations of interaction of GBs at time intervals as mentioned. Atoms are made invisible and only dislocations are shown after DXA. The green colored lines are dislocations with ⟨111⟩ Burgers vector, that of blue and pink colored are with Burgers vectors ⟨110⟩ and ⟨100⟩, respectively, and red for other Burgers vectors. The arrows in the dislocation lines indicate the direction of the Burgers vector. The defect not categorized as dislocations are shown as a grey-colored defect mesh. Simulations that had no dislocation activity are characterized using CNA. Atoms with eight neighbors (BCC atoms) are made invisible and other atoms are shown after CNA. (For interpretation of the references to color in this figure legend, the reader is referred to the web version of this article.)

The flow stress at 10% strain was about 755 MPa during compressive test carried out at strain rate of 10^{-2} s^{-1}. House et al. [49] carried out ECAP on Ta to a strain of 4. They found that the flow stress at strain rate of 10^{-1} s^{-1} and at 10% strain varied between 765 MPa and 900 MPa depending on whether the samples were taken from through thickness or in-plane directions. Maury et al. [89] obtained a maximum flow stress of 1160 MPa at 10^{-3} s^{-1}after 10 turns of HPT. The average grain diameter was reduced from initial 60 μm to 160 nm after 10 turns with ρ of ~1.4×10^{14} m^{-2}. In the current work, MAF of Ta after 9 passes ($\varepsilon_{eff} = 7.2$) gave a flow stress of 820 MPa in compression at a strain rate of 10^{-1} s^{-1}. The average grain diameter of 64 μm in Ta was reduced to 760 nm after 9 passes and had ρ of ~1.1×10^{14} m^{-2}.

R. Kapoor et al. carried out MAF of BCC Nb-1 wt% Zr which refined the grain from 100 to 1 μm and increased the strength from 120 to 540

MPa after 6th pass [16]. The strength increased by 4.5 times of the initial coarse-grained configuration. The calculated dislocation density was 3 $\times 10^{14}$ m^{-2}. Bhowmik et al. reported a study on MAF of a BCC IF steel up to 12 passes [24]. They achieved grain refinement from 225 to 0.3 μm after 12 passes. The dislocation density increased from 4.2 $\times 10^{13}$ to 1.3 $\times 10^{15}$ m^{-2} as obtained from X-ray diffraction line profile analysis. The yield strength of the IF steel increased from 105 to 600 MPa i.e. almost 6 times after 12 passes. In the current study after 6th pass, the grain size of 1.43 μm and yield strength of 613 MPa were obtained. The yield strength after 6 passes increased by 3.4 times of the initial coarse-grained configuration. The calculated dislocation density after 6th pass was 1.2 $\times 10^{14}$ m^{-2}. The difference in the increased strength after MAF between Nb-1 wt% Zr, IF steel and Ta could be due to the difference in the dislocation density and grain size. The current results on Ta are comparable to those of Nb-1 wt% Zr and IF steel, however the evolution of microstructure during MAF would be specific to the material depending on its alloying content, grain size, and dislocation density.

4.1. Contribution of dislocations and GBs to strength

The yield stress (σ_y) can be written as contributions from frictional stress (σ_0), strengthening due to dislocations ($\sigma_{dis} = \alpha MGb\sqrt{\rho}$) and strengthening due to GBs ($\sigma_{GB} = \frac{k_{HP}}{\sqrt{d_{GB}}}$) [17,90,91]. Thus, the yield strength is expressed as,

$$\sigma_y = \sigma_0 + \alpha MGb\sqrt{\rho} + \frac{k_{HP}}{\sqrt{d_{GB}}} \quad (4)$$

where α is a constant with a value of ≈ 0.2, and k_{HP} is the slope of the Hall–Petch plot. Taylor factor calculated from EBSD analysis for Ta is approximately taken as 3.2 [16]. For pure tantalum, σ_0 is 80 MPa, G is 69 GPa, b is 0.2863 nm, and k_{HP} is found using data points collected from references [92–96] as 438 MPa $\mu m^{0.5}$ [96,97]. Cordero et al. summarized the grain size data varying between 0.04 and 3900 for Ta using Hall-Petch relation [96]. The terms σ_0, α, M, G, b, and k_{HP} are constants, whereas the terms ρ and d_{GB} change with deformation and influence the yield stress.

The total dislocation density is a sum of statistically stored dislocations (SSD), GNDs, and dislocations that make up LAGBs. It was assumed that with strain, GNDs increase significantly as compared to the SSDs. The ρ_{GND} can be estimated using eq. 2 involving KAM, as mentioned in section 3.3. LAGB can provide strengthening either as grain boundaries or as dislocations, and that is specified by a critical misorientation angle φ_{dis}, such that boundaries with $\varphi > \varphi_{dis}$ (with area fraction f) contribute to the Hall-Petch term, whereas those with $\varphi < \varphi_{dis}$ (with area fraction 1-f) contribute to the dislocation hardening term. f can also be represented as d_R/d_{GB}, where d_R is the average grain diameter of all GBs and d_{GB} is the average grain diameter of those grains which contribute to GB hardening. In the present study, the median values obtained from Fig. 7a were d_R for each sample. Using this eq. 4 takes the following form:

$$\sigma_y = \sigma_0 + \alpha MGb\sqrt{\rho_{GND} + \frac{3(1-f)\varphi_{dis}}{bd_R}} + k_{HP}\sqrt{\frac{f}{d_R}}, \quad (5)$$

where φ_{dis} can take any value between 2° and 15°. Based on the previous experiments [50,69,91] when $\varphi_{dis} = 2°$ was used giving $f = 1$, eq. 5 reduced to eq. 4. This means that all boundaries ($\varphi > 2°$ – both LAGB and HAGB) contribute to grain boundary strengthening. Misorientations <2° are taken to be from GNDs which do not form boundaries and hence contribute to the dislocation strengthening term. The strengthening contributions from dislocation and GB for the case of $f = 1$ is plotted in Fig. 13a. The frictional stress is constant for all cases. The strengthening due to GB increased from CG to 9P.

The strengthening contributions from dislocation and GB for the case of $f = 1$ is plotted in Fig. 13a. The frictional stress is constant for all cases. The strengthening due to GB increased from CG to 9P. For the case when $\varphi_{dis} > 2°$, eq. 5 can be used with $f < 1$. To observe how a changing value of f affects each of the dislocation and GB strengthening terms and the total stress, Fig. 13b was plotted. Note that Fig. 13a is for $f = 1$. For lower values of f (Fig. 13b) (where some low angle boundaries start contributing to the dislocation strengthening term) the grain boundary strengthening term becomes less dominant and the dislocation hardening term increases. However, it is seen that for $f < 1$ the total stress predicted by eq. (5) is lower than that predicted for the case $f = 1$ and

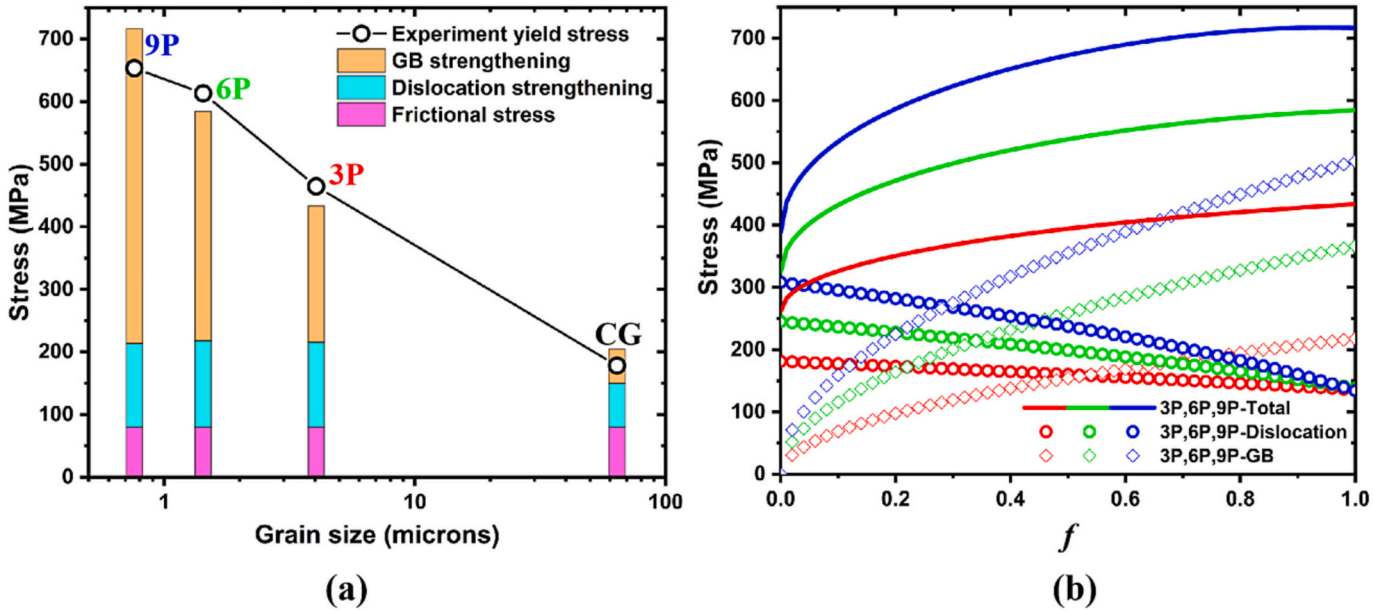

Fig. 13. (a) Calculated stress and experimental yield stress as a function of grain size for $\varphi_{dis} = 2°$. The experimental yield stress is represented by hollow circles connected by a line. The frictional stress, dislocation strengthening, and GB strengthening terms from the eq. 4 are stacked over one another. The overall height of the stacked column represented the calculated yield stress. The sample names are represented near to the stacked column. (b) Calculated total yield stress, dislocation strengthening, and GB strengthening terms as a function of f. The calculated yield stress is represented by solid lines, dislocation strengthening term is represented by hollow circles, and GB strengthening term is represented by hollow diamond symbols.

that of experiments. Thus, it can be inferred that the case of $f = 1$ best represents the contributions of hardening. This in turn implies that, apart from high angle boundaries, sub-grain boundaries too contribute to GB strengthening rather than to dislocation strengthening.

4.2. Grain refinement mechanism

Mechanisms of evolution of GBs during SPD have been explained using the transformation of dislocations or LAGBs or sub-structures to form HAGBs [30,50,51,98]. However, an understanding of the micro-mechanism of grain boundary movement and interactions is missing. In this work, MD simulations were used in studying the role of GBs during recrystallization and grain growth processes. In general, materials have a mixture of LAGBs, HAGBs and CSL GBs with random axis of rotation and misorientation between the grains. This is a complicated problem to model, however as a simplification the GBs can be modeled using tilt or twist of grains about an axis. In polycrystals, a grain has multiple neighbors that make different misorientation angles, thus resulting in different GB structures. In section 3.7.1, it was seen that the motion of LAGBs was favorable as compared to HAGBs. Although a direct comparison cannot be made of the experimental observations during MAF and MD simulations, the later was carried out to understand the motion of different types of grain boundaries under stress with an attempt to explain the experimentally observed microstructure. Here, simulations of shear deformation of asymmetric tilt GBs in conjunction with EBSD results were used to propose a mechanism for evolution of GBs during SPD. MD simulation showed that the GB motion was along the GB normal, while in earlier work on twist GBs it had been observed to be along tangential direction to GB plane [99]. Cahn proposed that the GB velocity v is a combined effect of coupling and sliding as $v = S\sigma + \beta v_n$ where S is the sliding factor, β is the coupling factor, v_n is normal component of velocity and σ is shear stress on GB. Cahn et al. [99] postulated that β is a function of misorientation between the grains and changes sign depending on the inclination angle in asymmetric GBs [77]. As it is difficult to determine S and β, in this study the dependence of mobility on driving pressure was used.

The proposed GB refinement model used the mobilities of the GBs and their interaction to solve for the evolution during MAF. The velocity (v) of a GB [53] is the product of the mobility of the GB (M_{gb}) and the driving pressure (P) i.e.

$$v = M_{gb}P. \tag{6}$$

The velocity of the GB depends on the stored energy in the system and on the force due to the external effects such as temperature and stress. The stored energy in the current configuration is the GBE and the external factor is the applied shear deformation. The mobility can be written using the Arrhenius equation as [53] $M_{gb} = M_0 e^{(-E_a/KT)}$ where M_0 is the reduced mobility and E_a is the activation energy to move the boundary. The effect of temperature is not studied in the current simulations. Using the driving pressure formulation in the current work, the effect of v, GBE, and θ on f_{hagb} was studied. The stored energy acting as driving pressure for an array of dislocations (such as in LAGBs) is given by [100].

$$P_{dis} = \frac{1}{2}\rho G b^2. \tag{7}$$

For any grain boundary, the stored energy acting as driving pressure is given by

$$P_{GB} = \frac{2\,GBE}{r_{GB}} \tag{8}$$

where r_{GB} is the radius of curvature of GB [100]. Flat GBs have $r_{GB} \to \infty$, so $P_{GB} \to 0$, i.e., no driving pressure. This confirms the necessity of formation of disconnections and ledges to mitigate the flatness of the GB. The presence of ledges in LAGBs ($\langle 112\rangle/16°$) and HAGBs ($\langle 112\rangle/23°$) induced curvature, but to find a value of the radius, the driving pressures of LAGBs were equated to that of GB, i.e. $P_{dis} = P_{GB}$. For GBs with dislocations the values of the radius were found to vary between 5 nm and 7.5 nm and an average value of 6 nm was used for calculation of GB mobility.

The shear stress was calculated during shear deformation of the GB configurations. The shear stress increased with initial shearing of the configuration. The value of the shear stress at the first drop in the shear stress can be attributed to the initial movement of GB and is termed as τ. The driving pressure due to τ is given by $P_\tau = 2\tau \cos\theta\, tan\left(\frac{\theta}{2}\right)$. For LAGBs, $P_\tau = \tau \sin\theta$ [101,102]. Since the current configurations have two GBs, P_τ was taken as

$$P_\tau = \tau \cos\theta \;\; \tan\left(\frac{\theta}{2}\right). \tag{9}$$

In the current study, it was assumed that the total driving pressure is due to both GBE (P_{GB}) and shear stress (P_τ). Thus the velocity of the GB can be summarized from the eq. 6–9 as

$$v = M_{gb}\left(\frac{2\,GBE}{r_{GB}} + \tau \cos\theta\, tan\left(\frac{\theta}{2}\right)\right) \tag{10}$$

where v, τ, GBE and their respective θ were from MD results. Using τ obtained from MD, the mobilities were calculated from eq. 10 and are plotted as function of θ in Fig. 14. It is seen that the mobility is high for LAGBs and decreases to a very low value for the HAGBs. Rahman also found that the mobility decreased from 4.7 m/s/MPa for $\theta = 7°$ to 1 m/s/MPa for $\theta = 23°$ [103]. Similar trend on mobility as a function of θ was observed by Olmsted et al. [104]. The categorization of GBs as a function of tilt angle in Fig. 14 was made using the behavior of the considered GBs during their initial movement as detailed in section 3.7.1.

Based on the above findings a model proposing the evolution of the microstructure with strain is schematically shown in Fig. 15. The initial microstructure primarily consists of grain with low dislocation density and HAGBs, some of which are immobile and some of which contain ledges (Fig. 15a). With increasing strain some GBs with ledges emit dislocations, some GBs dissociate into low angle boundaries with release

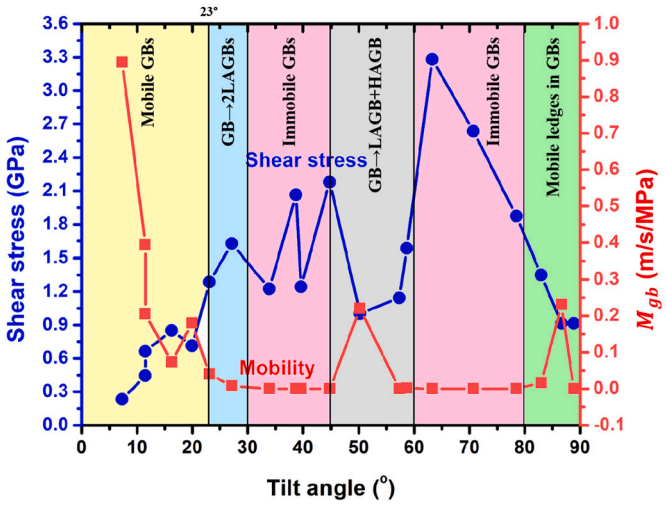

Fig. 14. Variation of shear stress obtained from MD simulations and mobility calculated from eq. 10 of GBs as a function of tilt angle. The regions of the plot are colored based on the mobility type of GBs. The yellow color is the region with dislocations in the mobile GB. The blue color is the region with GBs dissociating into two LAGBs and thus acquiring mobility. The pink color is the region with immobile GBs. The grey color is the region with GBs dissociating into LAGB and HAGB. The green color is the region with mobile ledges in GBs. (For interpretation of the references to color in this figure legend, the reader is referred to the web version of this article.)

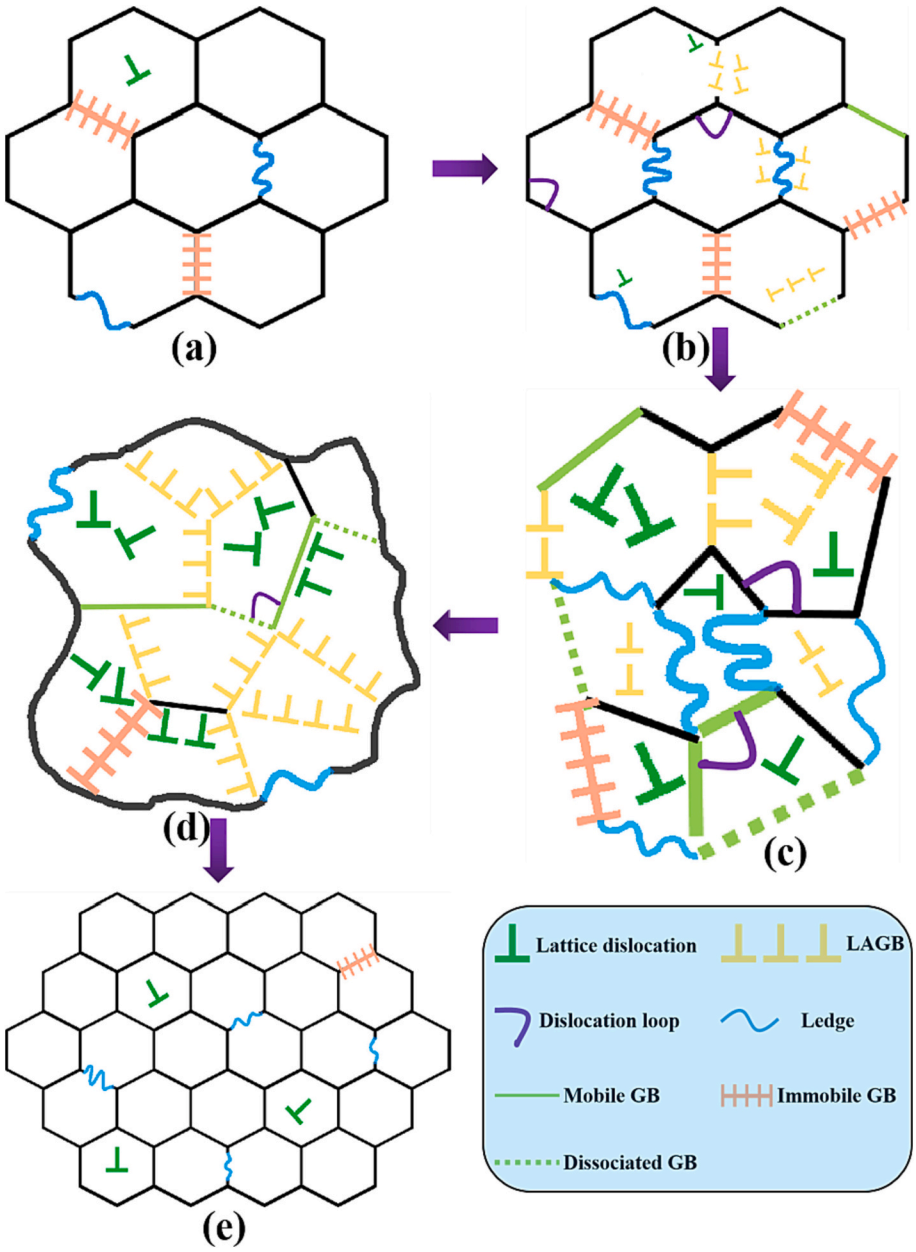

Fig. 15. Schematic illustration of grain refinement process during MAF. The various features such as lattice dislocations, dislocation loops, LAGBs, ledges, mobile GBs, immobile GBs, and dissociated GBs are represented by symbols as shown in legend.

of dislocations and dislocation loops in the grain (Fig. 15b). Dislocations interact and multiply within grains resulting in the increase of dislocation density leading to the formation of low angle boundaries. The above GB events reduce f_{hagb}. With further strain the above described mechanisms continue in addition to the migration of GBs (due to presence of LAGBs, ledges and some mobile HAGBs) (Fig. 15c). With further GB interactions, the dislocations and LAGBs arrange themselves to form sub-structure (Fig. 15d). With further strain LAGBs convert to HAGBs through the process of continuous dynamic recrystallization as described in earlier models [105] leading to a microstructure with grains having high angle boundaries and with low dislocation density within the grains (Fig. 15e).

5. Summary and conclusions

In the current experimental and simulation studies, the evolution of dislocations and GBs in pure Ta during MAF was investigated using various experimental characterizations and molecular dynamics technique. The important conclusions are listed below.

1. MAF of Ta increased the yield strength from 178 MPa (CG) to 653 MPa (9 pass) and hardness from 92 HV (CG) to 223 HV (9 pass) as a consequence of the increase in dislocation density and the formation of ultra-fine grains.
2. Grains were refined from 64 μm to 760 nm while dislocation density increased by an order of magnitude as compared to the initial CG. As the number of MAF passes increased, the fraction of recrystallized grains and HAGBs increased.
3. η and ε fibers were first observed in nucleated recrystallized grains after 3 passes along GBs of harder grains. After 9 passes, α and γ fibers were dominant.
4. The contribution of GB strengthening was higher than that of dislocation strengthening.

5. The mobility of the GBs dropped from around 1 m/s/MPa for LAGB to very low values for HAGBs with misorientation angle >23°.
6. The mobility of HAGBs with specific misorientations is either by dissociation to other GB types (between 30° and 45°) or a combined movement of ledges (between 80° and 90°). In either case, there is reduction in misorientation angle at the migrating location of the GBs.
7. The high mobility of LAGBs can be correlated with the recrystallization of grains with γ fibers by sub-structure formation process. The low mobility of HAGBs can be correlated with the recrystallization of grains having η and ε fibers by bulging and pinching process.

The experimental characterizations and relevant MD simulations of GB mobility provide insight and understanding into nanoscale features such as dislocations and GBs during SPD. Moreover, the correlation shown between EBSD and MD simulations lays a new path for experimental simulation linkage.

Supplementary data to this article can be found online at https://doi.org/10.1016/j.ijrmhm.2023.106120.

CRediT authorship contribution statement

A. Kedharnath: Conceptualization, Methodology, Investigation, Writing – original draft, Data curation, Software, Visualization. **Rajeev Kapoor:** Conceptualization, Investigation, Writing – review & editing, Supervision. **Apu Sarkar:** Conceptualization, Investigation, Writing – review & editing, Supervision.

Declaration of Competing Interest

The authors declare that they have no known competing financial interests or personal relationships that could have appeared to influence the work reported in this paper.

Data availability

Data will be made available on request.

Acknowledgment

This work was supported under the BARC 12th plan project number XII-N-R&D-25 'Experimental Studies for Ageing and Life Extension of Nuclear Components'. The authors thank Dr. R.N. Singh, Head Mechanical Metallurgy Division, BARC, for support and encouragement of this work.

References

[1] R.Z. Valiev, R.K. Islamgaliev, I.V. Alexandrov, Bulk nanostructured materials from severe plastic deformation, Prog. Mater. Sci. 45 (2000) 103–189, https://doi.org/10.1016/S0079-6425(99)00007-9.
[2] Y. Saito, H. Utsunomiya, N. Tsuji, T. Sakai, Novel ultra-high straining process for bulk MATERIALSÐDEVELOPMENT of the accumulative roll-bonding (arb) process, Acta Mater. 47 (1999) 579–583.
[3] E. Bruder, Formability of ultrafine grained metals produced by severe plastic deformation–an overview, Adv. Eng. Mater. 21 (2019) 1800316.
[4] R.Z. Valiev, I.V. Alexandrov, Y.T. Zhu, T.C. Lowe, Paradox of strength and ductility in metals processed by severe plastic deformation, J. Mater. Res. 17 (2002) 5–8, https://doi.org/10.1557/JMR.2002.0002.
[5] Y.J. Li, W. Blum, Strain rate sensitivity of cu after severe plastic deformation by multiple compression, Phys. Status Solidi Appl. Mater. Sci. 202 (2005) 119–121, https://doi.org/10.1002/pssa.200521160.
[6] R. Srinivasan, P.K. Chaudhury, B. Cherukuri, Q. Han, D. Swenson, P. Gros, Continuous severe plastic deformation processing of aluminum alloys, Final Tech. Rep. - Forg (2006) 1–59.
[7] R.Z. Valiev, Paradoxes of severe plastic deformation, Adv. Eng. Mater. 5 (2003) 296–300.
[8] R. Pippan, F. Wetscher, M. Hafok, A. Vorhauer, I. Sabirov, The limits of refinement by severe plastic deformation, Adv. Eng. Mater. 8 (2006) 1046–1056.
[9] M. Furukawa, Z. Horita, T.G. Langdon, Developing ultrafine grain sizes using severe plastic deformation, Adv. Eng. Mater. 3 (2001) 121–125.
[10] H.P. Stüwe, Equivalent strains in severe plastic deformation, Adv. Eng. Mater. 5 (2003) 291–295.
[11] T.C. Lowe, Y.T. Zhu, Commercialization of nanostructured metals produced by severe plastic deformation processing, Adv. Eng. Mater. 5 (2003) 373–378.
[12] S.M. Jagadeesh Babu, S.V.S. Narayana Murty, N. Prabhu, R. Kapoor, R.N. Singh, B.P. Kashyap, Effects of temporary alloying and severe plastic deformation on microstructure evolution and mechanical properties of Ti-alloys: a comparative study, Trans. Indian Inst. Metals 72 (2019) 1421–1425, https://doi.org/10.1007/s12666-019-01594-3.
[13] R. Kapoor, Severe Plastic Deformation of Materials, Elsevier, 2017, https://doi.org/10.1016/B978-0-12-801300-7.00020-6.
[14] S. Suwas, S. Mondal, Texture evolution in severe plastic deformation processes, Mater. Trans. 60 (2019) 1457–1471, https://doi.org/10.2320/matertrans.MF201933.
[15] D.J. Abson, J.J. Jonas, The hall-Petch relation and high-temperature subgrains, Met. Sci. J. 4 (1970) 24–28.
[16] R. Kapoor, A. Sarkar, A.N. Behera, S. Sunil, Multi-axial forging of Nb-1wt.%Zr: effect of annealing on microstructure and mechanical properties, Mater. Sci. Eng. A 772 (2020), 138805, https://doi.org/10.1016/j.msea.2019.138805.
[17] R. Kapoor, A. Sarkar, R. Yogi, S.K. Shekhawat, I. Samajdar, J.K. Chakravartty, Softening of Al during multi-axial forging in a channel die, Mater. Sci. Eng. A 560 (2013) 404–412, https://doi.org/10.1016/j.msea.2012.09.085.
[18] A. Kundu, R. Kapoor, R. Tewari, J.K. Chakravartty, Severe plastic deformation of copper using multiple compression in a channel die, Scr. Mater. 58 (2008) 235–238, https://doi.org/10.1016/j.scriptamat.2007.09.046.
[19] J.B. Singh, R. Kapoor, A. Durga Prasad, J.K. Chakravartty, Comparison of microstructures and strengths of an Al-2.5Mg alloy subjected to severe plastic deformation at room and liquid nitrogen temperatures, Mater. Sci. Eng. A 581 (2013) 26–30, https://doi.org/10.1016/j.msea.2013.05.073.
[20] S. Akbarian, A. Zarei-Hanzaki, H.R. Abedi, R. Unnikrishnan, R. Moat, Substructure development and deformation twinning stimulation through regulating the processing path during multi-axial forging of twinning induced plasticity steel, Adv. Eng. Mater. 20 (2018) 1–12, https://doi.org/10.1002/adem.201800453.
[21] S.K. Rajput, J. Kumar, Y. Mehta, T. Soota, K.K. Saxena, Microstructural evolution and mechanical properties of 316L stainless steel using multiaxial forging, Adv. Mater. Process. Technol. 6 (2020) 509–518, https://doi.org/10.1080/2374068X.2020.1728641.
[22] A.K. Padap, G.P. Chaudhari, V. Pancholi, S.K. Nath, Warm multiaxial forging of AISI 1016 steel, Mater. Des. 31 (2010) 3816–3824, https://doi.org/10.1016/j.matdes.2010.03.030.
[23] A.K. Padap, G.P. Chaudhari, S.K. Nath, V. Pancholi, Ultrafine-grained steel fabricated using warm multiaxial forging: microstructure and mechanical properties, Mater. Sci. Eng. A 527 (2009) 110–117, https://doi.org/10.1016/j.msea.2009.08.066.
[24] A. Bhowmik, S. Biswas, S.S. Dhinwal, A. Sarkar, R.K. Ray, D. Bhattacharjee, S. Suwas, Microstructure and texture evolution in interstitial-free (IF) steel processed by multi-axial forging, Mater. Sci. Forum 702–703 (2012) 774–777, https://doi.org/10.4028/www.scientific.net/MSF.702-703.774.
[25] Q. Chen, D. Shu, C. Hu, Z. Zhao, B. Yuan, Grain refinement in an as-cast AZ61 magnesium alloy processed by multi-axial forging under the multitemperature processing procedure, Mater. Sci. Eng. A 541 (2012) 98–104, https://doi.org/10.1016/j.msea.2012.02.009.
[26] S. Biswas, S. Suwas, Evolution of sub-micron grain size and weak texture in magnesium alloy mg-3Al-0.4Mn by a modified multi-axial forging process, Scr. Mater. 66 (2012) 89–92, https://doi.org/10.1016/j.scriptamat.2011.10.008.
[27] Z. Zhao, Q. Chen, C. Hu, D. Shu, Microstructure and mechanical properties of SPD-processed an as-cast AZ91D+Y magnesium alloy by equal channel angular extrusion and multi-axial forging, Mater. Des. 30 (2009) 4557–4561, https://doi.org/10.1016/j.matdes.2009.04.023.
[28] P. Trivedi, K.C. Nune, R.D.K. Misra, S. Goel, R. Jayganthan, A. Srinivasan, Grain refinement to submicron regime in multiaxial forged mg-2Zn-2Gd alloy and relationship to mechanical properties, Mater. Sci. Eng. A 668 (2016) 59–65, https://doi.org/10.1016/j.msea.2016.05.050.
[29] A. Salandari-Rabori, A. Zarei-Hanzaki, H.R. Abedi, J.S. Lecomte, H. Khatami-Hamedani, Micro and macro texture evolution during multiaxial forging of a WE43 magnesium alloy, J. Alloys Compd. 739 (2018) 249–259, https://doi.org/10.1016/j.jallcom.2017.12.181.
[30] Z. Hussain, F.A. Al-Mufadi, S. Subbarayan, O.M. Irfan, Microstructure and mechanical properties investigation on nanostructured nickel 200 alloy using multi-axial forging, Mater. Sci. Eng. A 712 (2018) 772–779, https://doi.org/10.1016/j.msea.2017.12.042.
[31] A. Shamsolhodaei, A. Zarei-Hanzaki, M. Moghaddam, Structural and functional properties of a semi equiatomic NiTi shape memory alloy processed by multi-axial forging, Mater. Sci. Eng. A 700 (2017) 1–9, https://doi.org/10.1016/j.msea.2017.04.011.
[32] N.M. Rusin, T.M. Poletika, S.L. Girsova, V.I. Danilov, Distinctive features of plastic strain localization under severe plastic deformation of metals, Russ. Phys. J. 50 (2007) 1111–1117, https://doi.org/10.1007/s11182-007-0163-8.
[33] S.M. Cardonne, P. Kumar, C.A. Michaluk, H.D. Schwartz, Tantalum and its alloys, Int. J. Refract. Met. Hard Mater. 13 (1995) 187–194, https://doi.org/10.1016/0263-4368(95)94023-R.
[34] R. Wauthle, J. Van Der Stok, S.A. Yavari, J. Van Humbeeck, J.P. Kruth, A. A. Zadpoor, H. Weinans, M. Mulier, J. Schrooten, Additively manufactured porous tantalum implants, Acta Biomater. 14 (2015) 217–225, https://doi.org/10.1016/j.actbio.2014.12.003.

[35] P. Kumar, C.E. Mosheim, Tantalum Base Alloys. https://patentimages.storage.googleapis.com/ad/26/23/af248d488dc227/US5633482.pdf, 1992.
[36] C.B.A. Forty, G.J. Butterworth, J.C. Sublet, Burnup of some refractory metals in a fusion neutron spectrum, J. Nucl. Mater. 212–215 (1994) 640–643, https://doi.org/10.1016/0022-3115(94)90137-6.
[37] R.W. Buckman Jr., New applications for tantalum and tantalum alloys, JOM. 52 (2000) 40–41.
[38] S.J. Zinkle, N.M. Ghoniem, Operating temperature windows for fusion reactor structural materials, Fusion Eng. Des. 51–52 (2000) 55–71, https://doi.org/10.1016/S0920-3796(00)00320-3.
[39] T.S. Byun, S.A. Maloy, Dose dependence of mechanical properties in tantalum and tantalum alloys after low temperature irradiation, J. Nucl. Mater. 377 (2008) 72–79, https://doi.org/10.1016/j.jnucmat.2008.02.034.
[40] S. Wurster, B. Gludovatz, A. Hoffmann, R. Pippan, Fracture behaviour of tungsten-vanadium and tungsten-tantalum alloys and composites, J. Nucl. Mater. 413 (2011) 166–176, https://doi.org/10.1016/j.jnucmat.2011.04.025.
[41] I. Ipatova, P.T. Wady, S.M. Shubeita, C. Barcellini, A. Impagnatiello, E. Jimenez-Melero, Radiation-induced void formation and ordering in ta-W alloys, J. Nucl. Mater. 495 (2017) 343–350, https://doi.org/10.1016/j.jnucmat.2017.08.029.
[42] S. Pappu, C. Kennedy, L.E. Murr, M.A. Meyers, Deformation twins in a shock-loaded ta-2.5w/oW precursor plate and a recovered, ta-2.5w/oW explosively formed penetrator, Scr. Mater. 35 (1996) 959–965, https://doi.org/10.1016/1359-6462(96)00248-5.
[43] D.S. Cowgill, Deformation behaviors of niobium and tantalum at low temperatures, Retrosp, Theses Diss (1964). https://lib.dr.iastate.edu/rtd/2654, 64—10,631.
[44] M. Schussler, Joppa, V.T. Bates, Tantalum-tungsten Alloy, 1971.
[45] W. Köck, P. Paschen, Tantalum-processing, properties and applications, Jom. 41 (1989) 33–39, https://doi.org/10.1007/BF03220360.
[46] R.J. Arsenault, An investigation of the mechanism of thermally activated deformation in tantalum and tantalum-base alloys, Acta Metall. 14 (1966) 831–838, https://doi.org/10.1016/0001-6160(66)90003-4.
[47] V. Stelmakh, V. Rinnerbauer, R.D. Geil, P.R. Aimone, J.J. Senkevich, J. D. Joannopoulos, M. Soljačić, I. Celanovic, High-temperature tantalum tungsten alloy photonic crystals: stability, optical properties, and fabrication, Appl. Phys. Lett. 103 (2013), https://doi.org/10.1063/1.4821586.
[48] N. Maury, N.X. Zhang, Y. Huang, A.P. Zhilyaev, T.G. Langdon, A critical examination of pure tantalum processed by high-pressure torsion, Mater. Sci. Eng. A 638 (2015) 174–182, https://doi.org/10.1016/j.msea.2015.04.053.
[49] J.O. Joel House, Philip Flater, Richard Harris, Robert De Angelis, Michael Nixon, John Bingert, Annealing and Mechanical Properties of ECAP Tantalum, 2011.
[50] R. Kapoor, A. Sarkar, R. Yogi, S.K. Shekhawat, I. Samajdar, J.K. Chakravartty, Softening of Al during multi-axial forging in a channel die, Mater. Sci. Eng. A 560 (2013) 404–412, https://doi.org/10.1016/j.msea.2012.09.085.
[51] S. Akbarian, A. Zarei-Hanzaki, H.R. Abedi, R. Unnikrishnan, R. Moat, Substructure development and deformation twinning stimulation through regulating the processing path during multi-axial forging of twinning induced plasticity steel, Adv. Eng. Mater. 20 (2018), https://doi.org/10.1002/adem.201800453.
[52] R. Kapoor, Severe plastic deformation of materials, in: Mater. Under Extrem. Cond. Recent Trends Futur. Prospect., 2017, https://doi.org/10.1016/B978-0-12-801300-7.00020-6.
[53] R.B. Godiksen, Z.T. Trautt, M. Upmanyu, J. Schiøtz, D.J. Jensen, S. Schmidt, Simulations of boundary migration during recrystallization using molecular dynamics, Acta Mater. 55 (2007) 6383–6391, https://doi.org/10.1016/j.actamat.2007.07.055.
[54] M.-W. Liu, M.P. Gururajan, K.-A. Wu, Morphological evolution of grain boundaries under lateral strains, Phys. Rev. Mater. 6 (2022), https://doi.org/10.1103/physrevmaterials.6.023601.
[55] A. Rajabzadeh, F. Mompiou, S. Lartigue-Korinek, N. Combe, M. Legros, D. A. Molodov, The role of disconnections in deformation-coupled grain boundary migration, Acta Mater. 77 (2014) 223–235, https://doi.org/10.1016/j.actamat.2014.05.062.
[56] A. Basak, A. Gupta, Simultaneous grain boundary motion, grain rotation, and sliding in a tricrystal, Mech. Mater. 90 (2015) 229–242, https://doi.org/10.1016/j.mechmat.2015.01.012.
[57] B. Beausir, J.J. Fundenberger, Analysis Tools for Electron and X-Ray Diffraction, ATEX—Software. www.Atex-Software.Eu, 2017.
[58] A. Kedharnath, A.S. Panwar, R. Kapoor, Molecular dynamics simulation of the interaction of a nano-scale crack with grain boundaries in α-Fe, Comput. Mater. Sci. 137 (2017) 85–99, https://doi.org/10.1016/j.commatsci.2017.05.026.
[59] A. Kedharnath, R. Kapoor, A. Sarkar, Classical molecular dynamics simulations of the deformation of metals under uniaxial monotonic loading: a review, Comput. Struct. 254 (2021), 106614, https://doi.org/10.1016/j.compstruc.2021.106614.
[60] A. Kedharnath, R. Kapoor, A. Sarkar, Atomistic simulation of interaction of collision cascade with different types of grain boundaries in α-Fe, J. Nucl. Mater. 523 (2019) 444–457, https://doi.org/10.1016/j.jnucmat.2019.06.021.
[61] D. Singh, A. Parashar, A. Kedharnath, R. Kapoor, A. Sarkar, Molecular dynamics-based simulations to study crack tip interaction with symmetrical and asymmetrical tilt grain boundaries in Zr, J. Nucl. Mater. 526 (2019), 151739, https://doi.org/10.1016/j.jnucmat.2019.151739.
[62] D. Singh, A. Parashar, A. Kedharnath, R. Kapoor, A. Sarkar, Effect of symmetrical and asymmetrical tilt grain boundaries on the tensile deformation of zirconium bicrystals: a MD-based study, J. Mater. Sci. 54 (2019) 3082–3095, https://doi.org/10.1007/s10853-018-3032-7.
[63] D. Frenkel, B. Smit, Understanding Molecular Simulation from Algorithms to Applications vol. 2, Academic Press, 2002. https://www.elsevier.com/books/understanding-molecular-simulation/frenkel/978-0-12-267351-1.
[64] A. Kedharnath, R. Kapoor, A. Sarkar, Effect of Tungsten Addition on Shock Loading Behavior in Ta–W System: A Molecular Dynamics Study, in: Adv. Struct. Integr., 2022, pp. 113–122, https://doi.org/10.1007/978-981-16-8724-2_11.
[65] S. Plimpton, Fast parallel algorithms for short-range molecular dynamics, J. Comput. Phys. 117 (1995) 1–19, https://doi.org/10.1006/jcph.1995.1039.
[66] E.N. Hahn, S.J. Fensin, T.C. Germann, M.A. Meyers, Symmetric tilt boundaries in body-centered cubic tantalum, Scr. Mater. 116 (2016) 108–111, https://doi.org/10.1016/j.scriptamat.2016.01.038.
[67] Y. Chen, J. Fang, L. Liu, W. Hu, N. Gao, F. Gao, H. Deng, Development of the interatomic potentials for W-ta system, Comput. Mater. Sci. 163 (2019) 91–99, https://doi.org/10.1016/j.commatsci.2019.03.021.
[68] R. Kapoor, N. Kumar, R.S. Mishra, C.S. Huskamp, K.K. Sankaran, Influence of fraction of high angle boundaries on the mechanical behavior of an ultrafine grained Al-mg alloy, Mater. Sci. Eng. A 527 (2010) 5246–5254, https://doi.org/10.1016/j.msea.2010.04.086.
[69] R. Kapoor, A. Sarkar, A.N. Behera, S. Sunil, Multi-axial forging of Nb-1wt.%Zr: effect of annealing on microstructure and mechanical properties, Mater. Sci. Eng. A 772 (2020), 138805, https://doi.org/10.1016/j.msea.2019.138805.
[70] G.I. Taylor, Plastic strain in metals, Twenty-Eighth May Lect. to Inst. Met. 62 (1938) 307–325.
[71] A. Das, Calculation of crystallographic texture of BCC steels during cold rolling, J. Mater. Eng. Perform. 26 (2017) 2708–2720, https://doi.org/10.1007/s11665-017-2695-6.
[72] C. Deng, S.F. Liu, J.L. Ji, X.B. Hao, Z.Q. Zhang, Q. Liu, Texture evolution of high purity tantalum under different rolling paths, J. Mater. Process. Technol. 214 (2014) 462–469, https://doi.org/10.1016/j.jmatprotec.2013.09.026.
[73] J. Baton, W. Geslin, C. Moussa, Influence of pre-recovery on the recrystallization of pure tantalum, J. Mater. Sci. 56 (2021) 15354–15378, https://doi.org/10.1007/s10853-021-06218-0.
[74] L. Jiang, M.T. Pérez-Prado, P.A. Gruber, E. Arzt, O.A. Ruano, M.E. Kassner, Texture, microstructure and mechanical properties of equiaxed ultrafine-grained Zr fabricated by accumulative roll bonding, Acta Mater. 56 (2008) 1228–1242, https://doi.org/10.1016/j.actamat.2007.11.017.
[75] S. Wang, Z.H. Wu, C. Chen, S.K. Feng, R. Liu, B. Liao, Z.H. Zhong, P. Lu, M. P. Wang, P. Li, J.W. Coenen, L.F. Cao, Y.C. Wu, The evolution of shear bands in ta-2.5W alloy during cold rolling, Mater. Sci. Eng. A 726 (2018) 259–273, https://doi.org/10.1016/j.msea.2018.04.059.
[76] A. Stukowski, Visualization and analysis of atomistic simulation data with OVITO-the open visualization tool, Model. Simul. Mater. Sci. Eng. 18 (2010), 015012, https://doi.org/10.1088/0965-0393/18/1/015012.
[77] Z.T. Trautt, A. Adland, A. Karma, Y. Mishin, Coupled motion of asymmetrical tilt grain boundaries: molecular dynamics and phase field crystal simulations, Acta Mater. 60 (2012) 6528–6546, https://doi.org/10.1016/j.actamat.2012.08.018.
[78] H. Song, J.J. Hoyt, A molecular dynamics simulation study of the velocities, mobility and activation energy of an austenite-ferrite interface in pure Fe, Acta Mater. 60 (2012) 4328–4335, https://doi.org/10.1016/j.actamat.2012.04.023.
[79] J.P. Hirth, R.C. Pond, Steps, dislocations and disconnections as interface defects relating to structure and phase transformations, Acta Mater. 44 (1996) 4749–4763, https://doi.org/10.1016/S1359-6454(96)00132-2.
[80] N. Combe, F. Mompiou, M. Legros, Multiple coupling modes to relax shear strain during grain boundary migration, Acta Mater. 218 (2021), 117222, https://doi.org/10.1016/j.actamat.2021.117222.
[81] D.A. Molodov, Microstructural Design of Advanced Engineering Materials, 2013, https://doi.org/10.1002/9783527652815.
[82] J.W. Cahn, Y. Mishin, A. Suzuki, Coupling grain boundary motion to shear deformation, Acta Mater. 54 (2006) 4953–4975, https://doi.org/10.1016/j.actamat.2006.08.004.
[83] S.V. Bobylev, I.A. Ovid'Ko, Stress-driven migration of deformation-distorted grain boundaries in nanomaterials, Acta Mater. 88 (2015) 260–270, https://doi.org/10.1016/j.actamat.2015.01.052.
[84] Y. Liu, S. Liu, C. Deng, H. Fan, X. Yuan, Q. Liu, Inhomogeneous deformation of {111}<uvw> grain in cold rolled tantalum, J. Mater. Sci. Technol. 34 (2018) 2178–2182, https://doi.org/10.1016/j.jmst.2018.03.015.
[85] J. Zhu, S. Liu, Y. Liu, N. Lin, S. Yang, C. Deng, Q. Liu, Deformation and annealing behavior in the 'interaction zone' of cold-rolled tantalum sheets, Vacuum. 164 (2019) 105–113, https://doi.org/10.1016/j.vacuum.2019.03.015.
[86] Y.H. Liu, S.F. Liu, J.L. Zhu, C. Deng, H.Y. Fan, L.F. Cao, Q. Liu, Strain path dependence of microstructure and annealing behavior in high purity tantalum, Mater. Sci. Eng. A 707 (2017) 518–530, https://doi.org/10.1016/j.msea.2017.09.097.
[87] M. Kazeminezhad, E. Hosseini, Modeling of induced empirical constitutive relations on materials with FCC, BCC, and HCP crystalline structures: severe plastic deformation, Int. J. Adv. Manuf. Technol. 47 (2010) 1033–1039, https://doi.org/10.1007/s00170-009-2239-9.
[88] Q. Wei, T. Jiao, S.N. Mathaudhu, E. Ma, K.T. Hartwig, K.T. Ramesh, Microstructure and mechanical properties of tantalum after equal channel angular extrusion (ECAE), Mater. Sci. Eng. A 358 (2003) 266–272, https://doi.org/10.1016/S0921-5093(03)00305-8.
[89] N. Maury, N.X. Zhang, Y. Huang, A.P. Zhilyaev, T.G. Langdon, A critical examination of pure tantalum processed by high-pressure torsion, Mater. Sci. Eng. A 638 (2015) 174–182, https://doi.org/10.1016/j.msea.2015.04.053.
[90] N. Hansen, Hall-petch relation and boundary strengthening, Scr. Mater. 51 (2004) 801–806, https://doi.org/10.1016/j.scriptamat.2004.06.002.

[91] N. Kamikawa, X. Huang, N. Tsuji, N. Hansen, Strengthening mechanisms in nanostructured high-purity aluminium deformed to high strain and annealed, Acta Mater. 57 (2009) 4198–4208, https://doi.org/10.1016/j.actamat.2009.05.017.
[92] M.B. Prime, A. Arsenlis, R.A. Austin, N.R. Barton, C.C. Battaile, J.L. Brown, L. Burakovsky, W.T. Buttler, S.-R. Chen, D.M. Dattelbaum, S.J. Fensin, D. G. Flicker, G.T. Gray, C. Greeff, D.R. Jones, J.M.D. Lane, H. Lim, D.J. Luscher, T. R. Mattsson, J.M. McNaney, H.-S. Park, P.D. Powell, S.T. Prisbrey, B. A. Remington, R.E. Rudd, S.K. Sjue, D.C. Swift, A broad study of tantalum strength from ambient to extreme conditions, Acta Mater. 231 (2022), 117875, https://doi.org/10.1016/j.actamat.2022.117875.
[93] M. Knezevic, I.J. Beyerlein, M.L. Lovato, C.N. Tomé, A.W. Richards, R.J. McCabe, A strain-rate and temperature dependent constitutive model for BCC metals incorporating non-Schmid effects: application to tantalum-tungsten alloys, Int. J. Plast. 62 (2014) 93–104, https://doi.org/10.1016/j.ijplas.2014.07.007.
[94] M. Kothari, L. Anand, Elasto-viscoplastic constitutive equations for polycrystalline metals: application to tantalum, J. Mech. Phys. Solids. 46 (1998) 51–67, https://doi.org/10.1016/S0022-5096(97)00037-9.
[95] G.Z. Voyiadjis, F.H. Abed, Microstructural based models for bcc and fcc metals with temperature and strain rate dependency, Mech. Mater. 37 (2005) 355–378, https://doi.org/10.1016/j.mechmat.2004.02.003.
[96] Z.C. Cordero, B.E. Knight, C.A. Schuh, Six decades of the Hall–Petch effect – a survey of grain-size strengthening studies on pure metals, Int. Mater. Rev. 61 (2016) 495–512, https://doi.org/10.1080/09506608.2016.1191808.
[97] F.J. Zerilli, R.W. Armstrong, Description of tantalum deformation behavior by dislocation mechanics based constitutive relations, J. Appl. Phys. 68 (1990) 1580–1591, https://doi.org/10.1063/1.346636.
[98] G. Wilde, J. Ribbe, G. Reglitz, M. Wegner, H. Rösner, Y. Estrin, M. Zehetbauer, D. Setman, S. Divinski, Plasticity and grain boundary diffusion at small grain sizes, Adv. Eng. Mater. 12 (2010) 758–764, https://doi.org/10.1002/adem.200900333.
[99] J.W. Cahn, J.E. Taylor, A unified approach to motion of grain boundaries, relative tangential translation along grain boundaries, and grain rotation, Acta Mater. 52 (2004) 4887–4898, https://doi.org/10.1016/j.actamat.2004.02.048.
[100] G. Gottstein, L.S. Shvindlerman, Grain Boundary Migration in Metals: Thermodynamics, Kinetics, Applications, 2nd ed, CRC Press, 2010, https://doi.org/10.1061/(asce)0733-9399(2000)126:8(888.
[101] D.A. Molodov, V.A. Ivanov, G. Gottstein, Low angle tilt boundary migration coupled to shear deformation, Acta Mater. 55 (2007) 1843–1848, https://doi.org/10.1016/j.actamat.2006.10.045.
[102] M. Winning, G. Gottstein, L.S. Shvindlerman, On the mechanisms of grain boundary migration, Acta Mater. 50 (2002) 353–363, https://doi.org/10.1016/S1359-6454(01)00343-3.
[103] M.J. Rahman, H.S. Zurob, J.J. Hoyt, A comprehensive molecular dynamics study of low-angle grain boundary mobility in a pure aluminum system, Acta Mater. 74 (2014) 39–48, https://doi.org/10.1016/j.actamat.2014.03.063.
[104] D.L. Olmsted, E.A. Holm, S.M. Foiles, Survey of computed grain boundary properties in face-centered cubic metals-II: grain boundary mobility, Acta Mater. 57 (2009) 3704–3713, https://doi.org/10.1016/j.actamat.2009.04.015.
[105] T. Sakai, A. Belyakov, R. Kaibyshev, H. Miura, J.J. Jonas, Dynamic and post-dynamic recrystallization under hot, cold and severe plastic deformation conditions, Prog. Mater. Sci. 60 (2014) 130–207, https://doi.org/10.1016/j.pmatsci.2013.09.002.